ELSEVIER

Peralkaline syenite autoliths from Kilombe volcano, Kenya Rift Valley: Evidence for subvolcanic interaction with carbonatitic fluids

Filippo Ridolfi [a,*], Alberto Renzulli [a], Ray Macdonald [b], Brian G.J. Upton [c]

[a] *Istituto di Scienze della Terra, Università degli Studi di Urbino Carla Bo, Campus Scientifico, I-61029 Urbino, Italy*
[b] *Environment Centre, Lancaster University, LA1 4YQ Lancaster, UK*
[c] *School of GeoSciences, University of Edinburgh, EH9 3JW Edinburgh, UK*

Abstract

Mineral chemistry, textures and geochemistry of syenite autoliths from Kilombe volcano indicate that they crystallized in the upper parts of a magma chamber from peralkaline trachytic magmas that compositionally straddle the alkali feldspar join in the "residuum system" (ne=0–1.03; qz=0–0.77). Mineral reaction and/or overgrowth processes were responsible for the replacement of (i) Mg–hedenbergite by aegirine–augite, Ca–aegirine and/or aegirine, (ii) fayalite by amphiboles, and (iii) magnetite by aenigmatite. Ti–magnetite in silica-saturated syenites generally shows ilmenite exsolution, partly promoted by circulating fluids.

By contrast, the Fe–Ti oxides in the silica-undersaturated (sodalite-bearing) syenites show no signs of deuteric alteration. These syenites were ejected shortly after completion of crystallization. Ilmenite–magnetite equilibria indicate fO_2 between -19.5 and -23.1 log units (T 679–578 °C), slightly below the FMQ buffer. The subsequent crystallization of aenigmatite and Na-rich pyroxenes suggests an increase in the oxidation state of the late-magmatic liquids and implies the influence of post-magmatic fluids.

Irrespective of silica saturation, the syenites can be divided into (1) "normal" syenites, characterized by Ce/Ce* ratios between 0.83 and 0.99 and (2) Ce-anomalous syenites, showing distinct negative Ce-anomalies (Ce/Ce* 0.77–0.24). "Normal" silica-saturated syenites evolved towards pantelleritic trachyte. The Ce-anomalous syenites are relatively depleted in Zr, Hf, Th, Nb and Ta but, with the exception of Ce, are significantly enriched in REE.

The silica-saturated syenites contain REE–fluorcarbonates (synchysite-bastnaesite series) with negative Ce-anomalies (Ce/Ce* 0.4–0.8, mean 0.6), corroded monazite group minerals with LREE-rich patches, and hydrated, Fe- and P-rich phyllosilicates. Each of these is inferred to be of non-magmatic origin. Fractures in feldspars and pyroxenes contain Pb-, REE- and Mn-rich cryptocrystalline or amorphous material. The monazite minerals are characterized by the most prominent negative Ce-anomalies (Ce/Ce$_{mean}$*=0.5), and in the most altered and Ca-rich areas (depleted in REE), Ce/Ce* is less than 0.2.

It is inferred that carbonatitic fluids rich in F, Na and lanthanides but depleted in Ce by fractional crystallization of cerian pyrochlore, percolated into the subvolcanic system and interacted with the syenites at the thermal boundary layers of the magma chamber, during and shortly after their crystallization.

Chevkinite–(Ce), pyrochlore, monazite and synchysite-bastnaesite, occurring as accessory minerals, have been found for the first time at Kilombe together with eudialyte, nacareniobsite–(Ce) and thorite. These latter represent new mineral occurrences in Kenya.
© 2006 Elsevier B.V. All rights reserved.

Keywords: Syenite; Carbonatite; Kilombe; Kenya rift valley; Ce-anomaly; REE–fluorcarbonate

* Corresponding author. Fax: +39 0722304245.
E-mail address: ridolfif@uniurb.it (F. Ridolfi).

1. Introduction

Within the Kenya Rift Valley, trachytes are important components of late Quaternary central volcanoes. For example, the caldera volcanoes Menengai, Longonot and Suswa, in the south-central rift (Fig. 1), are composed almost entirely of trachytes. However, basalts have been erupted between the centres and as mixed trachyte flows on Longonot (Scott, 1980; Rogers et al., 2004), suggesting that basalt is probably present beneath all the centres but has been unable to penetrate lower density trachytic caps.

It has been inferred that these late Quaternary centres are underlain by substantial magma chambers (Leat et al., 1984; Macdonald, 1987, 1994), and several studies have been aimed at understanding the processes operating within those chambers (Leat et al., 1984; Clarke et al., 1990; Macdonald et al., 1993, 1994).

An underutilised record of magma chamber processes are the suites of syenitic inclusions found, inter alia, at Menengai (Leat et al., 1984) and Longonot (Scott, 1980). The most extensive suite of such inclusions occurs at Kilombe, which is slightly older (~2 Ma; Jones, 1979a) than the geographically associated centres (Fig. 1; Rogers et al., 2004). These nodules almost certainly represent the crystallization products of trachytic magmas in a high-level reservoir (Jones, 1979a) and should be regarded as autoliths rather than xenoliths.

In this paper, we document the mineral chemistry and geochemistry of the Kilombe syenites and provide
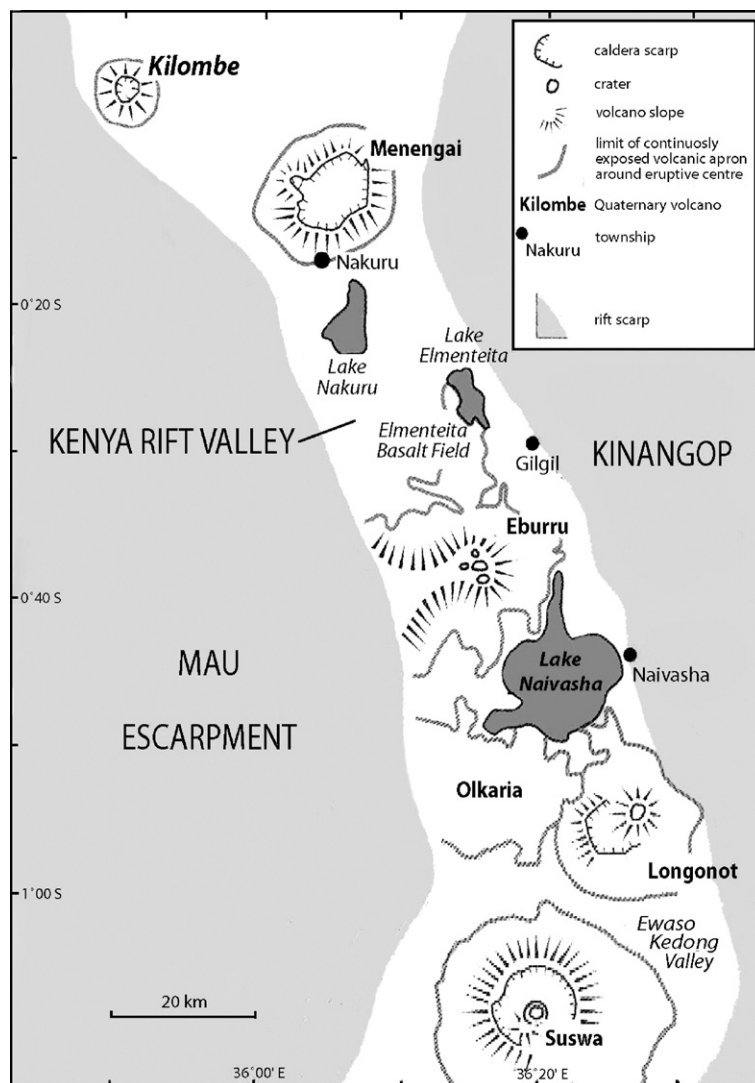

Fig. 1. Location of the Kilombe volcano in the Kenya Rift Valley.

evidence of interaction between the syenites and carbonatitic fluids, emphasizing the role of CO_2 and REE in trachytic magmatism of the rift. We also report on the unusual suite of accessory minerals in the syenites.

2. Geological summary

The Kilombe (or Eldalat) caldera volcano is situated on the western inner flank of the Kenya Rift Valley at the junction of the Kenya and Kavirondo rifts (35°50′E, 0°05′S; Fig. 1). It has a volume of 15 km³ and is formed almost entirely of trachyte lavas and pyroclastic flows (McCall, 1964). Trachytic tuffs partially fill the caldera and Jones (1979b) has reported four mixed benmoreite–trachyte flows that overlie the Saos Mugearite, which comprises alkali basalts, hawaiites and mugearites (McCall, 1964).

The syenites occur as inclusions up to 5 cm in two post-caldera flows but up to 20 cm in the caldera-filling tuff. However, boulders up to several metres across are distributed over the outer slopes up to 2 km from the caldera, being most abundant on the south side (Jones, 1979a).

3. Analytical methods

Whole-rock analyses on 20 selected samples were carried out at the Activation Laboratories Ltd (Ancaster, Canada). Major and trace element concentrations were determined using a Thermo Jarrell-Ash ENVIRO II (ICP-OES) and a Perkin Elmer SCIEX ELAN 6000 (ICP-MS), respectively. The analytical methodologies and errors are reported in Ridolfi et al. (2003).

Samples selected for analysis by scanning electron microscope and electron microprobe are K4, K7, K16, K18, K20, K21, K22, K23 and K24.

Back-scattered electron (BSE) imaging and qualitative composition of the minerals was conducted at the University of Roma Tre (Italy), using an SEM Philips XL30-super UTW instrument.

Quantitative mineral compositions were determined with the electron probe micro-analyser (EPMA) Cameca SX-100 (WDS) of the School of GeoSciences, University of Edinburgh (UK). Natural silicates and metals and synthesized glasses of known composition were used as standards. Operating conditions were 20 keV, 20 nA for fundamental minerals and 40 nA for phases containing elements with atomic number ≥ 39 (i.e., Y). WDS qualitative spectra were performed for each mineralogical species to detect the elements contained and to set up the analytical files before the runs. Analyses were

carried out in spot mode (beam size ~ 1 μm) or rastering the beam in square areas up to 100 μm² to minimize the loss of Na from the less stable minerals such as eudialyte and nacareniobsite–(Ce). Analytical errors depend on the absolute abundances of each element. EPMA relative errors of the oxide are estimated to be $<1\%$ at the >10 wt.% level, $5-10\%$ at the 1 wt.% level, $10-20\%$ at the $0.2-1$ wt.% level, and $20-40\%$ at the <0.1 wt.% level.

4. Petrography

Jones (1979a) divided the syenite autoliths of Kilombe and of the nearby Londiani volcano into four groups:

(1) most abundant, and forming all the large blocks (up to some metres), are coarse-grained syenites. These are thought to have formed by nearly complete solidification of batches of trachytic melt, although a small proportion of residual liquid may have been lost;
(2) fine-grained syenites, representing essentially solidified trachytic magma;

Table 1
Modal compositions of the syenite autoliths from Kilombe

Group	SiO₂-saturated syenites	SiO₂-undersaturated syenites
Samples	K1–K15, K17–K21, K23–K27	K16, K22
Modal mineralogy (vol.%)		
Alkali feldspar	84.5–95.0	85.5–86.5
Quartz	≤3.0	–
Sodalite	–	1.5–3.5
Analcime	≤2.0	–
Amphibole	0.5–6.0	1.0–1.5
Pyroxenes	1.5–8.0	5.0–6.0
Annite	≤1.0	<0.5
Altered phyllosilicate	≤3.5	<0.5
Fe–Ti oxides	≤2.5	≤2.5
Fayalite	≤1.0	–
Aenigmatite	0.5–3.0	1.0
Zircon	<0.5	–
Eudialyte	–	<0.5
Nacareniobsite–(Ce)	–	<0.5
Chevkinite–(Ce)	<0.5	–
Pyrochlore	<0.5	<0.5
Pyrite	–	<0.5
Apatite	≤1.0	<0.5
Monazite	<0.5	–
Xenotime	<0.5	–
Thorite	<0.5	–
REE–fluorocarbonates	<0.5	–
Clay alteration	From absent to elevated	Absent

(3) aplitic syenites occurring as veins in the other syenite types, also interpreted by Jones (1979a) as representing trachyte magma;

(4) dark green melasyenites, found in very late-stage post-caldera tuffs, interpreted as crystallization products of Na–Fe–Nb–Y–REE-enriched residual liquids from the coarser grained syenites.

Groups 1 and 2 are dominated by alkali feldspars and characterized by primary olivine, hornblende, Fe–Ti oxides, ferroaugite and nepheline. Interstitial phases include aenigmatite, katophorite, arfvedsonite, hydroannite, apatite, aegirine and quartz or analcime. Feldspar crystal sizes range from ∼5 mm in the coarse-grained syenites to ∼0.5 mm in the finer grained syenites. The
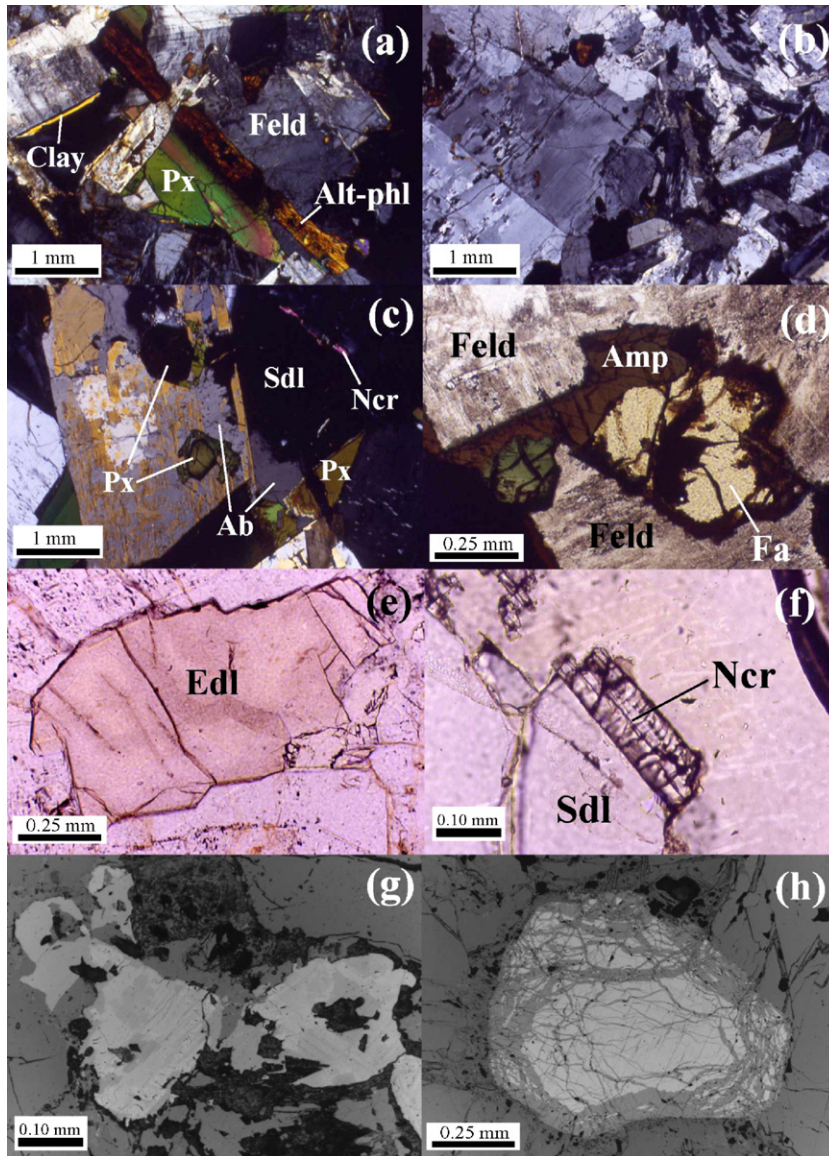

Fig. 2. Photomicrographs showing representative textures of the Kilombe syenites. Crossed nicols: (a) randomly disposed feldspars (Feld) interlocked with altered phyllosilicates (Alt-phl), interstitial pyroxenes (Px) and void spaces partly filled by clay minerals (Clay) (sample K23); (b) boundary area between fine- and coarse-grained feldspars (sample K20); (c) pyroxene (Px) inclusions in the primary feldspars which are partly replaced by albite (Ab) that also fills the cavities and interstitial crystals of sodalite (Sdl) and nacareniobsite–(Ce) (Ncr) (sample K16). Parallel nicols: (d) fayalite (Fa) in the interstices between feldspars (Feld) with reaction/overgrowth of brown amphibole (Amp) (sample K24); (e) interstitial crystal of eudialyte (Edl) (sample K16); (f) nacareniobsite–(Ce) (Ncr) in a cavity at the edge of sodalite (Sdl) (sample K16). Reflected-light: (g) re-homogenization by fluids of lamellar structures in the magnetites (sample K10); (h) magnetite enclosed in an aenigmatite crystal, showing edge and irregular veins of reaction with the magma (sample K22).

aplitic veins consist of 50–70% albite, 20–30% aegirine and 0–30% quartz. The melasyenites are characterised by aegirine needles poikilitically enclosed in large albite crystals.

All the samples in this study are coarse-grained syenites, but none carries nepheline. Here, the syenite autoliths are divided into (1) SiO_2-saturated syenites (±modal quartz); (2) SiO_2-undersaturated, sodalite-bearing syenites. One syenite (K24) of the SiO_2-saturated group contains modal analcime as a result of post-magmatic processes. Modal compositions of each syenite group, determined by counting ~800 points, are reported in Table 1. The samples consist mainly of crystals of interlocked and randomly oriented feldspars, with lengths between 3.5 and 10 mm (Fig. 2a). Sample K20 has feldspars of variable sizes, zones characterized by smaller feldspars (average ~1.0 mm) and coarser grained parts (Fig. 2b). The feldspars vary from glassy-clear to altered, opaque white crystals. All the syenites are holocrystalline–hypidiomorphic and the feldspar–feldspar grain boundaries are locally consertal. Sub-rounded, polygonal to triangular, void spaces make up 1–10 vol.%. Alkali feldspars were strongly affected by fluid circulation leading to vein and patch perthites (sensu Smith and Brown, 1988, Shelley, 1992). In the sodalite-bearing syenites, the feldspars are partly replaced by albite that, in general, fills the cavities (Fig. 2c). Alteration of alkali feldspars to clay minerals varies from zero (K12, K13, K20, K25, K27) to almost 100% in the SiO_2-saturated syenites. Some also show clay minerals partly filling cavities (Fig. 2a). Clayey alteration is diffuse in the analcime-bearing sample (K24) but absent in the sodalite-bearing syenites (Table 1).

The phyllosilicates are totally altered to brown or greenish-brown, euhedral or anhedral pseudomorphs, showing prominent cleavage (Fig. 2a). Pyroxenes are usually zoned or show overgrowths of aegirine–augite or aegirine. Fayalite crystals in the interstices between feldspars are partly replaced by amphibole (Fig. 2d). In the sodalite-bearing syenites, eudialyte and nacareniobsite–(Ce) crystallized in cavities together with sodalite (Fig. 2c, e, f). REE–fluorcarbonates of the synchysite–bastnaesite series are present in the silica-saturated syenites, but absent from the sodalite-bearing syenites (Table 1).

Magnetites in most of the syenites contain exsolved ilmenite lamellae, suggesting a protracted cooling history in the subvolcanic system. Re-homogenization of lamellar structures in roundish magnetite grains occurs in the interstices or in inclusions crossed by fractures (Fig. 2g). In the sodalite-bearing syenites

Table 2

Representative microprobe analyses of mafic minerals: 1–4 pyroxene, 5–8 amphibole, 9–13 Fe–Ti oxides, 14–15 aenigmatite

Spot	1	2	3	4	5	6	7	8	9	10	11	12	13	14	15
Sample	K22	K16	K20	K21	K22	K7	K18	K18	K20	K22	K20	K20	K22	K22	K20
Mineral	Mg-hdn	Aeg-aug	Ca-aeg	Aeg	Ktp	Ktp	Fe-frn	Arf	Ilm	Ilm	Usp	Mgn	Mgn	Ang	Ang
Type	–	–	–	–	–	–	–	–	exsolv.	prim.	exsolv.	exsolv.	prim.	–	–
SiO_2	49.67	49.63	50.88	52.00	44.66	46.29	47.50	52.22	0.08	0.05	1.27	0.91	0.20	38.21	42.19
TiO_2	0.56	0.35	1.05	2.15	1.43	2.82	0.49	0.01	45.26	51.21	21.98	0.04	9.83	8.45	9.61
ZrO_2	0.04		4.48	0.02	0.12	0.05	0.93	0.03							
Al_2O_3	0.60	0.69	0.38	1.19	5.13	2.47	2.25	0.04	0.08	0.04	0.10	0.04	0.10	1.97	0.13
MgO	6.18	1.98	0.06	0.21	6.00	1.33	2.72	7.25	0.19	0.05	0.08	0.06	0.02	0.49	0.33
CaO	20.56	17.52	2.88	0.19	7.39	3.98	1.43	1.45						1.46	0.03
MnO	1.07	1.13	1.18	0.33	1.10	1.39	2.24	1.99	4.38	5.51	2.32	0.56	1.76	1.32	5.98
FeO_{tot}	20.47	25.21	26.39	27.87	25.47	31.65	30.48	25.55	48.46	42.68	64.13	92.69	82.28	41.79	35.72
BaO									1.02		0.51	0.04			
Na_2O	0.68	3.26	11.69	13.52	4.70	6.60	8.05	8.71						6.27	7.35
K_2O					1.68	1.54	1.54	0.94							
F					0.70	0.82	0.75	1.49							
Sum					98.38	98.93	98.37	99.68	–	–	–	–	–	–	–
O=F	–	–	–	–	−0.30	−0.34	−0.31	−0.63	–	–	–	–	–	–	–
Total	99.83	99.76	99.00	97.49	98.08	98.59	98.06	99.05	99.47	99.53	90.40	94.32	94.18	99.95	101.32
Mg#	0.38	0.17	0.02	0.43	0.30	0.07	0.16	0.35	–	–	–	–	–	–	–
K_{alk}	–	–	–	–	–	–	–	–	–	–	–	–	–	19.2	22.2

Blank=below EMP detection limit. Mg-hdn=magnesian hedenbergite; Aeg-aug=aegirine–augite; Ca-aeg=calcium aegirine; Aeg=aegirine; Ktp=katophorite; Fe-frn=ferric ferronyböite; Arf=arfvedsonite; Ilm=ilmenite; Usp=ulvospinel; Mgn=magnetite; Ang=aenigmatite; exsolv.=exsolved; prim.=primary; K_{alk}=alkalinity modulus (see text).

(K16, K22), the magnetites show no ilmenite exsolution, implying that these rocks were expelled from the subvolcanic system shortly after complete solidification. Nevertheless, magnetite crystals enclosed in aegirine and aenigmatite show edges and irregular veins indicative of reaction with peralkaline melt (Fig. 2h).

5. Mineral chemistry

Representative compositions of pyroxene, amphibole, Fe–Ti oxides, aenigmatite, eudialyte, nacareniobsite–(Ce), rinkite, pyrochlore, thorite, xenotime, monazite, cheralite and synchysite–bastnaesite series are shown in Table 2 and 3. A complete set of mineral analyses and formulae is presented as electronic supplement (Supplement 1).

5.1. Feldspar

The primary feldspars in the syenites were significantly affected by the post-magmatic circulation of fluids, characterized by Na enrichment through $K^+ \rightarrow Na^+$ exchange (Figs. 2a–c). Thus, the bulk composition of the original feldspars cannot be obtained by calculation from image processing–quantitative

Table 3

Representative microprobe analyses of accessory phases: 1–2 eudialyte, 3–5 rinkite group, 6–8 pyrochlore, 9 thorite, 10 xenotime, 11–13 monazite group, 14–16 synchysite–bastnaesite series

Spot	1	2	3	4	5	6	7	8	9	10	11	12	13	14	15	16
Sample	K16	K16	K16	K16	K16	K20	K16	K23	K23	K24	K24	K4	K20	K24	K20	K24
Mineral	Edl	Edl	Ncr	Ncr	Rnk	Prc	Prc	Prc	Thr	Xnt	Mnz	Chr	Mnz	Syn	Prs	Bst
Type	–	–	–	–	–	–	–	–	–	–	unalt.	alt.	alt.	–	–	–
P_2O_5									0.04	27.21	27.77	25.01	28.96	0.31	0.17	
Nb_2O_5	0.50	0.63	10.08	9.42	4.95	51.98	59.29	50.41								
Ta_2O_5						3.51	0.96	1.27								
SiO_2	50.49	48.64	29.21	29.54	29.58		6.48		19.57	1.51	1.47	1.86	3.56	0.12	0.18	0.22
TiO_2	0.00	0.00	1.64	1.99	4.48	5.64		7.14								
ZrO_2	11.84	12.15	0.17	0.26	0.60	0.66	0.29	0.83	0.11							
ThO_2						0.31	0.10	0.99	79.50	3.41	0.45	29.17	0.05			
UO_2						2.77	2.24	0.91	1.07							
Al_2O_3	0.17	0.25														
Y_2O_3	0.96	0.91	2.15	1.76	1.60				0.67	35.75	1.57	4.31	4.74	5.37	1.10	0.65
La_2O_3	0.56	0.69	4.48	4.54	4.04	2.47	1.25	4.64		0.03	20.06	4.48	21.53	8.45	13.79	18.01
Ce_2O_3	0.91	1.10	7.21	9.19	8.98	4.71	1.53	9.14		0.16	27.56	4.25	6.96	19.73	25.50	33.75
Pr_2O_3			1.16	1.51	1.56	0.81	0.06	1.56		0.02	4.59	1.52	6.64	9.23	3.96	11.43
Nd_2O_3	0.38	0.49	2.35	3.49	4.22	1.66	0.24	3.09		0.63	8.81	4.16	14.07	3.14	8.98	5.29
Sm_2O_3			0.32	0.61	0.74					1.11	1.88	0.73	1.82	1.66	1.55	1.39
Gd_2O_3			0.86	1.11	1.20					4.07	3.57	0.99	2.16	3.09	3.21	3.34
Dy_2O_3										7.26						
CaO	8.62	9.00	22.15	20.35	21.54	8.89	14.69	4.68		0.26	0.49	6.59	2.90	16.25	9.12	0.30
MnO	3.59	1.25	0.06	0.24	0.38											
FeO	5.06	6.59	0.62			0.15		3.04								
PbO						0.79		0.18								
Na_2O	14.47	13.61	9.29	8.29	7.99	6.12	7.53	4.60								
K_2O	0.46	0.39									0.27	0.23	0.04			
F	0.33	0.08	6.47	5.62	6.29	2.64	4.40	2.53		0.89	0.88	0.29	0.70	4.81	1.43	6.82
Cl	1.35	1.72														
CO_2[a]	–	–	–	–	–	–	–	–	–	–	–	–	–	28.99	29.32	22.22
Sum	99.66	97.49	97.61	97.90	98.16	93.57	99.20	95.00	100.95	82.30	99.36	83.60	94.14	101.15	98.32	103.42
O=F, Cl	− 0.44	− 0.42	− 2.73	− 2.37	− 2.65	− 1.11	− 1.85	− 1.06	0.00	− 0.37	− 0.37	− 0.12	− 0.29	− 2.02	− 0.60	− 2.87
Total	99.22	97.07	94.89	95.53	95.51	92.46	97.35	93.94	100.95	81.93	98.99	83.47	93.85	99.13	97.71	100.55
K_{alk}	33.6	32.8	33.9	31.2	30.4	–	–	–	–	–	–	–	–	–	–	–
Ce/Ce*	1.22	1.21	0.72	0.81	0.83	0.77	0.83	0.78	–	–	0.64	0.37	0.13	0.45	0.79	0.52
La/Nd$_N$	2.86	2.67	3.63	2.47	1.83	2.83	10.02	2.86	–	–	4.33	2.05	2.91	5.12	2.92	6.49

Blank=below EMP detection limit. [a]CO_2 calculated by charge balance. Edl=eudialyte, Ncr=nacareniobsite–(Ce), Rnk=rinkite, Prc=pyrochlore, Thr=thorite; Xnt=xenotime; Mnz=monazite; Chr=cheralite; Syn=synchysite; Prs=parisite; Bst=bastnaesite; unalt.=unaltered; alt.=altered; K_{alk}=alkalinity modulus (see text); Ce/Ce*=Ce/(La+Pr)/2 normalized to chondrites; La/Nd$_N$=La/Nd normalized to chondrites (Nakamura, 1974).

analysis of exsolved phases (Marks and Markl, 2001; Marks et al., 2003). Analyses made in patches with different BSE brightness indicate a continuous compositional range ($Ab_{16–99}Or_{1–84}An_{0–2}$). The average anorthoclase varies from $Ab_{57}Or_{43}$ to $Ab_{62}Or_{38}$ in the silica-saturated samples (K7, K18, K20 and K21) and is $Ab_{61}Or_{39}$ in the sodalite-bearing syenite K22.

5.2. Pyroxene

According to Rock's (1990) classification, the pyroxene crystallization trend is from magnesian hedenbergite ($En_{20}Fs_{33}Wo_{47}–En_5Fs_{45}Wo_{50}$), through aegirine–augite and calcian aegirine to aegirine ($Jd_{1–7}Aeg_{17–96}Quad_{2–80}$; Table 2 and Supplement 1). The most Mg-rich magnesian hedenbergites are found as inclusions in the alkali feldspars of the silica-undersaturated syenite K22, whilst the interstitial pyroxenes with elevated Na content, close to the aegirine end-member, occur in the most peralkaline syenites (i.e., K7; see Chap. 6). Zoned crystals show similar patterns. ZrO_2 (0–4.5%) and TiO_2 (0.2–3.8%) contents usually increase from crystal cores to rims. Kilombe pyroxenes in the Di–Hed–Aeg system show Aeg increase in conjunction with drops in diopside and hedenbergite (Fig. 3). The Hed percentage correlates

positively with the degree of SiO_2 saturation in the syenites (Fig. 3a), perhaps due to lower f_{O_2} values in the SiO_2-rich magmas favouring the crystallization of Fe^{2+}-rich pyroxenes (i.e., hedenbergite). This behaviour is compared to the pyroxene patterns in extrusive rocks (comendites and pantellerites) and syenite autoliths (quartz-bearing, sodalite-bearing and nepheline syenites) (Fig. 3b) representing peralkaline magmas with different silica saturation.

5.3. Amphibole

Based on the Leake et al. (1997) classification, amphiboles in the silica-saturated syenites vary from Na–Ca-rich types (katophorite; $Na_B = 0.5–1.5$) to Na-rich compositions (ferric ferronyböite to arfvedsonite; $Al^{VI} < Fe^{3+}$, $Na_B > 1.5$). In almost all the analysed amphiboles, the transition to arfvedsonitic compositions reflects an increase of Si and Na in the magma (Table 2 and Supplement 1). By contrast, the sodalite-bearing sample K22 contains only katophorites characterized by low Si content (Si = 6.9–7.1 apfu) and elevated Mg# (0.29–0.32), unlike the Na–Ca amphiboles in the silica-saturated syenites (Si = 7.1–7.6 apfu, Mg# = 0.05–0.21). The presence in the amphiboles of narrow zones with variable Na, Ca, F and Fe^{3+}/Fe^{2+} ratios (Fig. 4) may
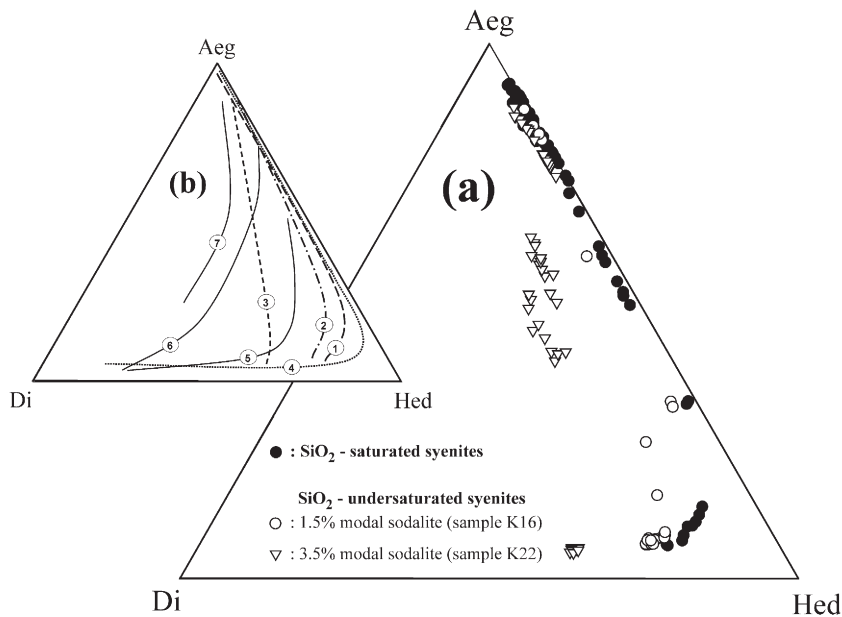

Fig. 3. (a) Pyroxene compositions in the ternary system diopside (Di), hedenbergite (Hed) and aegirine (Aeg); (b) trends of pyroxene of the Kilombe syenites reported in (a): SiO$_2$-saturated (curve 1), sodalite-bearing K16 (curve 2) and K22 (curve 3) syenites; worldwide comendite–pantellerite volcanic rocks (curve 4); peralkaline SiO$_2$-saturated syenites (curve 5) and sodalite-bearing syenites (curve 6) of Agua de Pau (Azores); agpaitic nepheline syenite of Tenerife (curve 7). Data source: 1, 2 and 3: this paper; 4: Nicholls and Carmichael (1969), Macdonald et al. (1987) and Scaillet and MacDonald (2003); 5 and 6: Ridolfi et al. (2003); 7: Wolff (1987) and Ridolfi (2004). See text for further explanations.
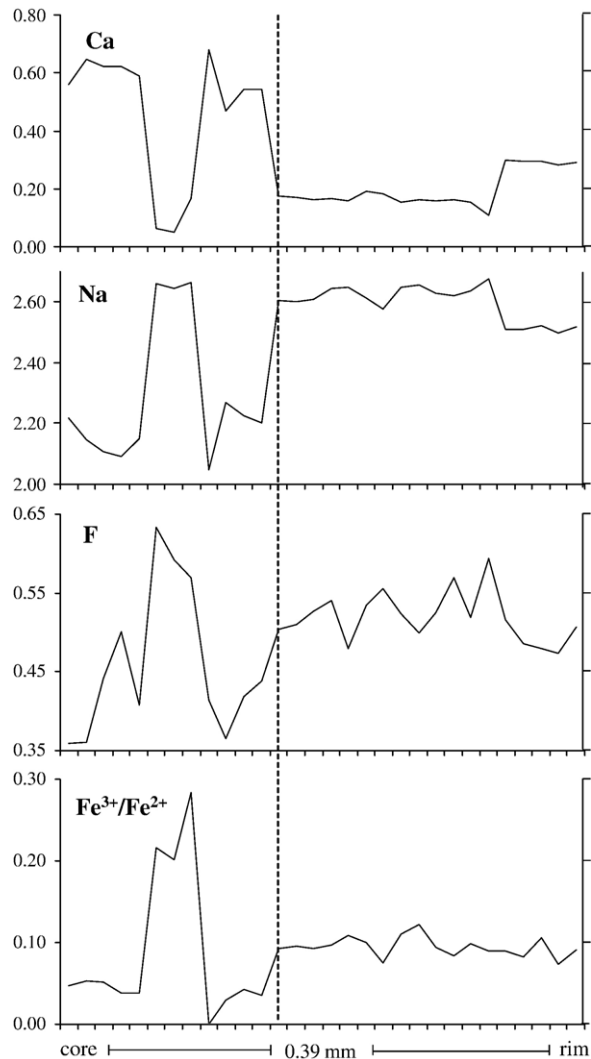
Fig. 4. Variation profile of Ca, Na, F and Fe^{3+}/Fe^{2+} ratio in an amphibole ranging from ferric ferronyböite (core) to arfvedsonite (rim). The broken line separates the two amphibole species in the same crystal (sample K7). 30 spot analyses were carried out along the crystal transect.

reflect transient changes in the element activity, fluorine and oxygen fugacity of the magma during crystal growth.

5.4. Fe–Ti oxides

As noted above, ilmenite exsolved from titanomagnetite in the silica-saturated syenites but not in the silica-undersaturated group. Table 2 reports representative analyses of exsolved and primary oxides. Primary ilmenite shows little variation, from $Ilm_{84}Prf_{12}$ to $Ilm_{89}Prf_6$ (Emt ~5% and Gkl close to zero in both), whereas exsolved crystals are characterized by a larger range ($Ilm_{67}Gkl_1Prf_8Emt_{24}$–$Ilm_{87}Gkl_0Prf_{11}Emt_2$; Supplement 1).

The spinels in the exsolved phases vary from ulvöspinel ($Mgn_{45}Usp_{55}$) to pure magnetite (Mgn=100), with a spinel component up to 1%, whilst the silica-undersaturated syenites contain only magnetites ($Mgn_{59}Usp_{41}$–$Mgn_{83}Usp_{17}$). In the ilmenite of sample K20, BaO values reach 1.2% and some re-homogenized magnetites show total oxides down to 92.2%, even after Fe_2O_3/FeO calculation (Supplement 1). The low totals may suggest the incorporation of H_2O in the magnetite lattice promoted by post-magmatic fluids.

5.5. Fayalite

The early fayalite crystals show fairly constant compositions ($Fo_4Fa_{90}Tp_6$).

5.6. Annite

Phyllosilicates can show structural vacancies up to 1 apfu (Rieder et al., 1998). This is the case with the analysed annites of Kilombe ($Phl_{2-16}Ann_{84-98}$), where the oxide sums are low (93.1%), possibly as result of fluid alteration. As F (0.1–0.8%) is negatively correlated with total oxides, the fluids are assumed to have been F-rich.

5.7. Aenigmatite

Aenigmatite is normally found in silica-saturated and silica-undersaturated peralkaline rocks (e.g., Deer et al., 1966; Abbott, 1967; Wallace et al., 1990; Dawson, 1997; Kunzmann, 1999; Ridolfi et al., 2003). The substitution $Si^{4+} \rightarrow Al^{3+}$ in the fourfold coordinated site is more favoured in aenigmatites of the sodalite-bearing syenites K16 and K22 (Al_2O_3 0.5–2.5%; MnO 1.3–2.8%) than those of the silica-saturated group (Al_2O_3 0.1–0.9%) showing greater $Fe^{2+} \rightarrow Mn^{2+}$ exchange (MnO 2.7–7.9%; Table 2, Supplement 1). Zonation is absent. A useful parameter characterizing the alkaline tendency of Zr–Ti–Nb silicates in peralkaline (agpaitic) rocks is the "alkalinity modulus" K_{alk} (Khomyakov, 1995; Ridolfi et al., 2003), i.e., the percentage of alkali/ (alkali+Si+Al and its substitutes) in the mineral formulae. In the Kilombe aenigmatites, K_{alk} ranges between 19.2% and 22.2% (Table 2, Supplement 1).

5.8. Eudialyte

Eudialyte is a Na-rich zirconosilicate in the homonymous group of minerals (Johnsen and Grice, 1999; Johnsen et al., 2001). Table 3 shows two representative eudialyte compositions whereas Supplement 1 gives

further analyses, formulae and the mean of 26 spots of a ~2-mm interstitial crystal in a sodalite-bearing syenite (K16; Fig. 2e). SiO_2 (48.6–50.5%), ZrO_2 (11.7–12.4%), Na_2O (13.1–14.5%), CaO (7.9–9.0%) and FeO (5.1–6.8%) are in the range of the 36 eudialyte analyses compiled by Johnsen and Gault (1997). Chlorine (1.2–1.5 apfu) is more abundant than F (0–0.9 apfu). The formulae closely resemble the eudialyte end-member $Na_{15}Ca_6Fe_3Zr_3Si(Si_{25}O_{73})(O,OH,H_2O)_3(Cl,OH)_2$ (Stromeyer, 1819; Johnsen et al., 2001). Slight variations (Nb 0.1–0.3 apfu, Mn 0.5–1.6 apfu) can be related to eudialyte–kentbrooksite solid solution (Johnsen et al., 1998). K_{alk} lies between 31.7% and 33.6% (average 32.8%) close to the alkalinity modulus of ideal eudialyte (34.1%). Calcium is replaced in minor amounts by the LREE (La 0.1–0.2 apfu, Ce 0.2–0.3 apfu, Nd 0.1 apfu). There is modest LREE enrichment (La/Nd_N 1.9–3.0, mean 2.2; Table 3, Supplement 1 and Fig. 5).

5.9. Nacareniobsite–(Ce)

Nacareniobsite–(Ce) is a rare Na-rich niobiosilicate in the rinkite group (Slepnev, 1957), distinguishable from the other members of the series (i.e., rinkite–johnstrupite–rinkolite–lovchorrite) in having Nb/Ti > 1.0 [ideally, $NbNa_3Ca_3REE(Si_2O_7)_2OF_3$; Petersen et al., 1989]. As with eudialyte, nacareniobsite–(Ce) was only found in the sodalite-bearing syenites (sample K16); it displays low total oxides (94.9–96.6%) and crystallized during the very late magmatic stages (Figs. 2c, f, 6a). Supplement 1 gives representative compositions of 31 minerals of the rinkite group. Compared to the average of 10 nacareniobsite–(Ce) analyses reported by Petersen et al. (1989), most crystals exhibit higher percentages of ZrO_2 (0.2–1.8%), CaO (20.4–22.3%) and Y_2O_3 (1.6–2.2%) and lower contents of Nb_2O_5 (7.1–10.1%) and Na_2O (8.3–9.3%). The Kilombe nacareniobsite–(Ce) also contains Gd_2O_3
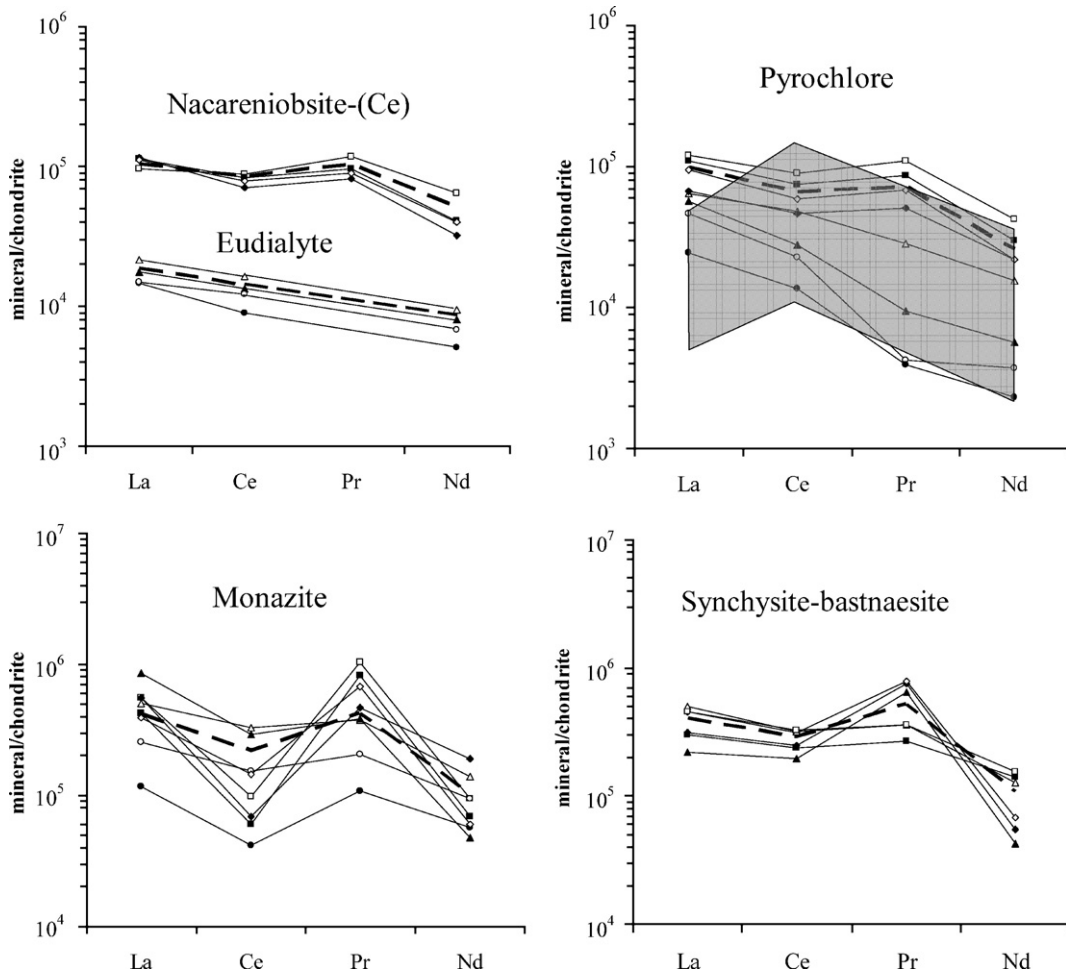

Fig. 5. Representative LREE patterns of minerals normalized to chondrites (Nakamura, 1974). The broken lines indicate average compositional patterns. The field covered by carbonatite magmatic pyrochlores (grey) is reported for comparison (Wagner et al., 2003).
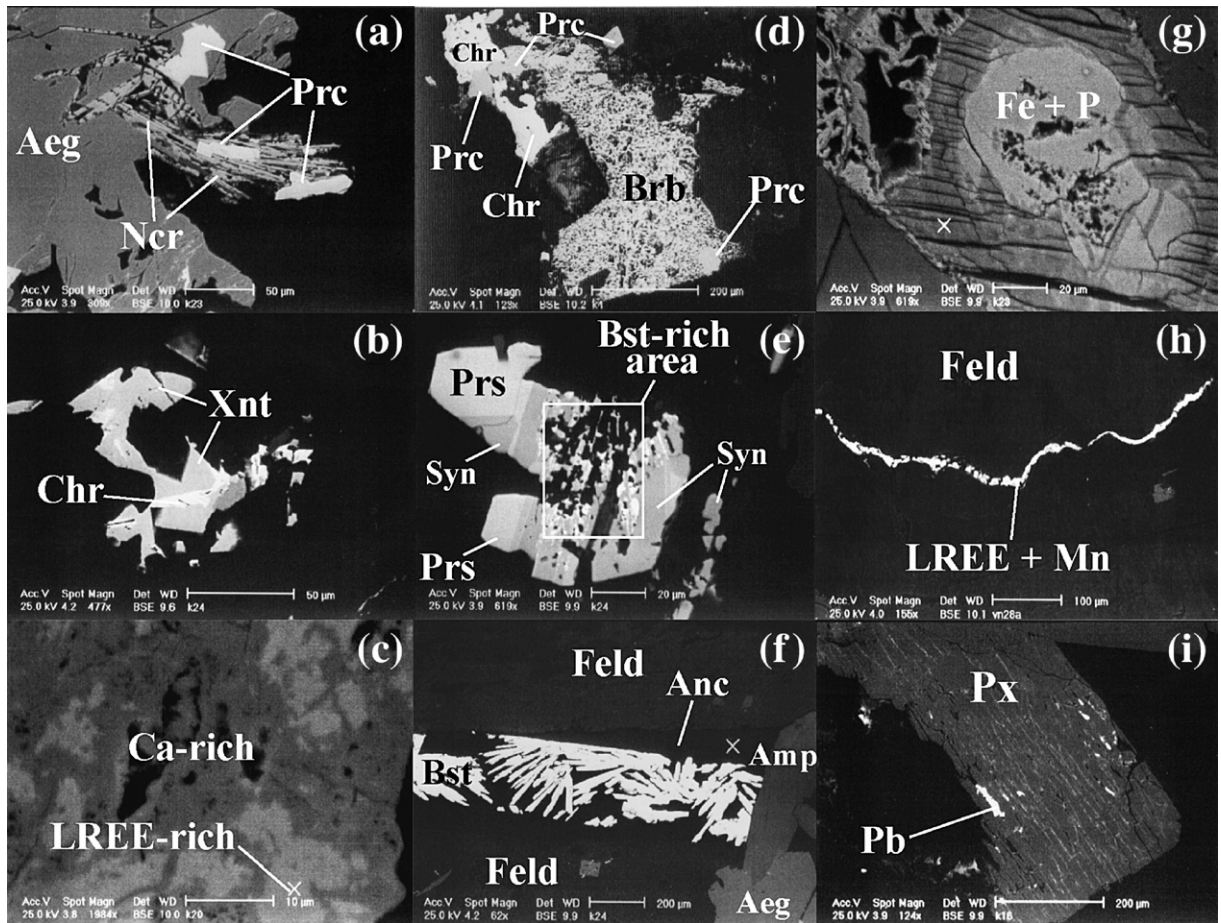
Fig. 6. SEM-BSE images of (a) bright pyrochlores (Prc) and acicular nacareniobsite–(Ce) (Ncr) enclosed at the rim of an aegirine (Aeg) crystal (sample K16); (b) xenotime (Xnt) crystals partially replaced by cheralite (Chr) (sample K24); (c) monazite crystal showing areas with different LREE/Ca ratios (sample K20); (d) alteration of an unknown phase (presumably monazite) into acicular crystals of brabantite (Brb) close to pyrochlores (Prc) and cheralites (Chr) (sample K4); (e) thick intergrowth of minerals of the synchysite (Syn)–parisite (Prs)–bastnaesite (Bst) series (sample K24); (f) variolitic crystals of bastnaesite (Bst) enclosed poikilitically by analcime (Anc); feldspar (Feld) and amphibole (Amp) are also present (sample K24); (g) altered phyllosilicate enriched in Fe and P (sample K20); (h) fracture in alkali feldspar (Feld) filled by LREE- and Mn-rich material (sample K20); (i) fractures and irregular cleavages in pyroxene crystal filled by Pb-rich material (sample K16).

from 0.9% to 1.2%. Only one crystal shows Nb/Ti < 1 and closely resembles the rinkite formula [TiNa$_2$Ca$_4$REE (Si$_2$O$_7$)$_2$OF$_3$; Supplement 1]. In this mineral, K_{alk} drops to 30.4%, i.e., 7.1% lower than the alkalinity modulus of the nacareniobsite–(Ce) end-member (37.5%), but very close to ideal rinkite K_{alk} (28.6%). Fig. 5 emphasizes the low negative Ce-anomaly (Ce/Ce* 0.72–0.88, mean 0.82) and weak LREE fractionation (La/Nd$_N$ 1.5–3.6, mean 2.0), similar to those of eudialyte (Table 3; Supplement 1).

5.10. Chevkinite–(Ce)

Back-scattered imaging and qualitative EDS analyses revealed the presence in the silica-saturated sample K23 of rare interstitial crystals of a LREE–Fe–Ca-rich titanosilicate closely resembling chevkinite–(Ce) (Macdonald and Belkin, 2002). The small size and the low stability of the minerals under the electron beam did not allow quantitative analyses.

5.11. Pyrochlore

On the basis of the major B-site cations, Hogarth (1977) divided pyrochlores into three subgroups: microlite (Nb + Ta > 2Ti, Ta > Nb), pyrochlore (Nb + Ta > 2Ti, Nb > Ta) and betafite (2Ti > Nb + Ta).

As for many igneous rocks (e.g., Hogarth, 1989; Kovalenko et al., 1995; Lumpkin and Ewing, 1996; Chakhmouradian and Mitchell, 1998, 2002; Uher et al., 1998; Chakhmouradian and Sitnikova, 1999;

Stähle et al., 2002), the Kilombe syenites contain minerals of the pyrochlore subgroup (Nb 1.6–1.7 apfu, Ti 0.2–0.4 apfu, Ta 0.0–0.1 apfu; Supplement 1). The B site has low contents of Zr (ZrO_4 0.2–1.7%). As no distinctive element exceeds 0.4 apfu in the A site, all the minerals are pyrochlore. CaO (4.7–14.7%) always exceeds Na_2O (4.6–8.6%) and the A sites contain variable amounts of rare earths (REE_2O_3 2.5–19.2%) and lower contents of Th (ThO_2 0–1.7%) and U (UO_2 0.9–3.6%). FeO_{tot} is between 0.1% and 3.7%. Although LREE patterns show both negative and positive Ce-anomalies the negative ones predominate (Ce/Ce* 0.70–1.14, mean 0.77). By contrast pyrochlore from carbonatites are characterized by a significant positive Ce-anomaly (Fig. 5). La/Nd$_N$ ratios are, on the average (mean 3.8), higher than those of eudialyte and nacareniobsite–(Ce) (Table 3; Supplement 1).

5.12. Thorite and xenotime

Table 3 reports two compositions of thorite ($ThSiO_4$) and xenotime (YPO_4) in the syenites. These are isostructural and can show solid solution with zircon ($ZrSiO_4$) and coffinite ($USiO_4$) (Pointer et al., 1988). In late-magmatic crystals of thorite, small amounts of U (UO_4 1.0–1.9%), Y (Y_2O_3 0.5–1.8%) and Zr (ZrO_4 0.1–0.4%) replace Th (ThO_4 76.1–79.5%), while the substitution of Si for P is very low ($P_2O_5 \leq 0.4\%$; Supplement 1).

There is weak $(Y+MREE)+P \rightarrow Th+Si$ substitution in the xenotime (ThO_2 2.5–3.8%; SiO_2 1.0–1.5%). BSE analysis reveals that xenotime has been partly replaced by cheralite (Fig. 6b) through fluid interaction. Consequently, the analyses show very low total oxides (81.9–83.9%), implying the incorporation of large amounts of volatiles (i.e., H_2O and CO_2), F (0.9–1.4%) and CaO (0.1–0.4%). In addition, small contents of $LREE_2O_3$ (1.9–4.1%) have replaced Y_2O_3 (34.2–38.1%) and $MREE_2O_3$ (11.8–13.1%) (Supplement 1).

5.13. Monazite

Minerals of the monazite group, with the general formula ABO_4, lie within the ternary system monazite ($LREEPO_4$)–brabantite [$CaTh(PO_4)_2$]–huttonite ($ThSiO_4$) (Bowie and Horne, 1953). There is wide solid solution between the three, with intermediate species such as cheralite, (LREE, Th, Fe Ca) (P,Si)O_4 (e.g., Bowie and Horne, 1953; Della Ventura et al., 1996). BSE studies in the silica-saturated syenites show that the monazites underwent extensive post-magmatic alteration. At high magnifications, they commonly display both irregular corrosion cavities as

a result of fluid interactions and patchy zones with unchanged LREE-rich contents (Fig. 6c). Very small needles of brabantite replace a previous interstitial phase but the alteration does not seem to affect the enclosed or nearby crystals of pyrochlore and cheralite (Fig. 6d). The monazite-group minerals are either unaltered with total oxides ∼100%, or altered, where totals drop to 77.2% (Table 3; Supplement 1). Similar by low total monazites were reported in the supergene lanthanide mineralization of the Buru carbonatite centre, Western Kenya (Onuonga and Bowden, 2000). According to the dominant REE (Levinson's rule), most of the unaltered crystals are monazite–(Ce), whereas a few are monazite–(La) (Ce_2O_3 27.6–34.3%; La_2O_3 15.3–32.9%). Total REE oxides vary from 66.5% to 74.0%. ThO_2, SiO_2 and Y_2O_3 reach 5.7%, 2.1% and 1.6%, respectively, and CaO is <0.5%. By contrast, the altered monazites, despite low total oxides, typically show higher percentages of SiO_2 (≤ 7.2), ThO_2 (≤ 29.9), Y_2O_3 (≤ 8.2) and CaO (0.1–6.6), and a wider range of La/Ce ratios (0.3–3.1). These increases are balanced by lower P_2O_5 (23.6–30.5%) and REE_2O_3 (16.1–61.4%). A secondary crystal shows a cheralite–(La) composition. Brabantite crystals were not analysed because of their small size and instability.

Monazites are characterized by a variety of LREE patterns (Fig. 5), presumably due to various magmatic and post-magmatic (fluid) contributions. In fact, La/Nd$_N$ (1.9–18.0, mean 4.0) and Ce/Ce* ratios (0.10–0.86, mean 0.53) are very variable for all the analysed monazites (Supplement 1).

5.14. Synchysite–parisite–bastnaesite series

REE–fluorcarbonates of the synchysite [$REECaF(CO_3)_2$]–parisite [$CaREE_2(CO_3)_3F_2$]–bastnaesite [$REE(CO_3)F$] series, very common in differentiated carbonatites and hydrothermal assemblages (e.g., Hogarth, 1989; Onuonga and Bowden, 2000; Smith et al., 2000), have also been found as syn- or post-magmatic minerals in several types of syenites (e.g., Chakhmouradian and Mitchell, 1998; Förster, 2000; Isobe, 2000). The hydrothermal origin of the REE–fluorcarbonates found in the Kilombe syenite autoliths is indicated by thick intergrowths and corrosion phenomena among the members of this series. Sample K24 shows crystals of bastnaesite within interstitial post-magmatic analcime (Fig. 6f).

Table 3 and Supplement 1 give compositions of this series in K24 and K20 syenite autoliths. Both samples contain all the members of the series [i.e., synchysite–

Table 4
Whole-rock chemical analyses and CIPW normative compositions of the syenite autoliths of Kilombe

Group	"Normal" syenites										Ce-anomalous syenites									
Sample	K27	K25	K1	K22	K9	K23	K24	K4	K12	K7	K26	K2	K5	K3	K8	K6	K10	K21	K18	K20
Element as oxides (wt.%)																				
SiO_2	62.49	62.68	61.67	61.61	61.95	61.90	62.16	62.42	62.57	60.67	62.40	61.38	63.10	61.26	62.02	62.42	63.04	61.50	62.47	62.31
TiO_2	0.88	0.65	0.83	0.66	0.67	0.56	0.58	0.39	0.49	0.53	0.91	0.68	0.50	0.71	0.68	0.65	0.59	0.67	0.64	0.60
Al_2O_3	16.00	16.07	15.29	15.67	15.43	15.22	15.34	15.19	14.90	13.83	16.77	16.14	16.70	16.00	16.32	16.22	16.48	15.94	15.75	15.20
Fe_2O_3	7.23	6.49	7.56	7.07	6.84	7.29	7.52	6.52	7.66	10.02	6.17	6.15	5.03	6.68	6.51	6.12	5.33	6.23	6.41	7.25
MnO	0.21	0.24	0.30	0.22	0.23	0.25	0.26	0.26	0.29	0.36	0.17	0.17	0.16	0.26	0.22	0.19	0.17	0.23	0.26	0.27
MgO	0.10	0.22	0.31	0.30	0.10	0.15	0.13	0.20	0.24	0.17	0.08	0.24	0.10	0.31	0.15	0.20	0.19	0.17	0.30	0.35
CaO	0.48	0.56	0.84	0.95	0.32	0.50	0.84	0.52	0.66	0.61	0.19	0.59	0.29	0.61	0.41	0.59	0.58	0.45	0.78	0.94
Na_2O	6.82	6.86	6.72	7.44	7.29	7.13	7.62	7.28	7.43	7.47	6.83	6.43	7.16	6.37	6.68	6.79	6.84	6.86	6.89	6.96
K_2O	5.25	5.42	5.41	5.10	5.17	5.28	4.89	5.30	5.12	4.79	5.34	5.44	5.23	5.84	5.61	5.55	5.74	5.34	5.56	5.08
P_2O_5	0.03	0.03	0.02	0.06	0.02	0.04	0.05	0.03	0.03	0.03	0.05	0.03	0.05	0.04	0.03	0.03	0.03	0.04	0.03	0.12
TTEO	0.20	0.19	0.24	0.21	0.20	0.31	0.28	0.27	0.23	0.23	0.14	0.17	0.18	0.20	0.17	0.20	0.18	0.23	0.23	0.42
LOI	0.78	1.07	0.99	0.38	1.76	1.04	0.70	1.83	0.31	1.12	1.08	1.92	1.28	1.48	1.30	1.01	1.00	2.19	0.57	1.08
Total	100.48	100.48	100.17	99.67	99.98	99.66	100.38	100.21	99.92	99.83	100.14	99.34	99.78	99.75	100.11	99.97	100.16	99.85	99.89	100.58
REE_2O_3	0.04	0.04	0.03	0.04	0.04	0.05	0.06	0.07	0.05	0.05	0.05	0.04	0.07	0.04	0.03	0.04	0.04	0.06	0.06	0.21
PI	1.06	1.07	1.11	1.13	1.14	1.15	1.16	1.17	1.19	1.26	1.01	1.02	1.04	1.05	1.05	1.06	1.06	1.07	1.10	1.11
qz	0.17	–	–	–	–	–	–	0.77	0.59	0.08	0.17	0.26	–	–	–	–	–	–	–	0.03
ne	–	–	–	1.03	–	–	–	–	–	–	–	–	–	–	–	–	–	–	–	–
ac	4.12	4.96	6.90	6.45	6.31	6.70	6.84	6.00	6.97	9.21	1.13	1.52	3.42	3.71	3.42	4.40	4.52	5.25	5.84	6.61
ns	–	–	0.14	0.83	0.98	0.95	1.20	1.50	1.62	2.02	–	–	–	–	–	–	–	–	0.40	0.37
Eu/Eu*	0.38	0.48	0.56	0.34	0.35	0.30	0.27	0.33	0.32	0.24	0.36	0.45	0.35	0.45	0.63	0.48	0.50	0.35	0.42	0.29
Ce/Ce*	0.83	0.99	0.99	0.93	0.89	0.93	0.92	0.92	0.85	0.91	0.24	0.64	0.32	0.36	0.77	0.68	0.77	0.73	0.40	0.44
La/Nd$_N$	2.88	3.21	3.55	2.72	3.27	3.28	2.76	3.04	3.21	3.85	3.60	3.16	3.65	3.82	3.33	3.23	3.16	3.17	3.36	4.10

The samples are presented in order of increasing peralkalinity index (PI) in each group. Some CIPW normative minerals (qz, ne, ac and ns) are also shown. TTEO=total trace element oxides. Eu/Eu*=Eu/(Sm+Gd)/2, Ce/Ce*=Ce/(La+Pr)/2, La/Nd$_N$=La/Nd (values normalized to chondrites; Nakamura, 1974).

(Ce)–parisite–(Ce)–bastnaesite–(Ce)], where Ce_2O_3 (19.7–33.8%) always exceeds La_2O_3 (8.4–19.3%). Nevertheless, the negative Ce-anomaly is significant in the minerals of both samples (Ce/Ce* = 0.43–0.84, mean = 0.66). In these REE–fluorcarbonates, the Ce/Ce* ratio decrease is accompanied by enrichment in Pr and decrease in Nd (Fig. 5), consistent with the La/Nd_N increase (2.0–7.2, mean 3.8).

5.15. Other alteration features

Fluid–rock interactions are also inferred from crypto-crystalline or amorphous deposits in the major minerals. Thus, altered phyllosilicates carry irregular corrosion zones enriched in Fe and P (Fig. 6g), whereas fractures and cleavage in the feldspars and pyroxenes contain LREE-, Mn- and Pb-rich filling materials (Figs. 6h, i).
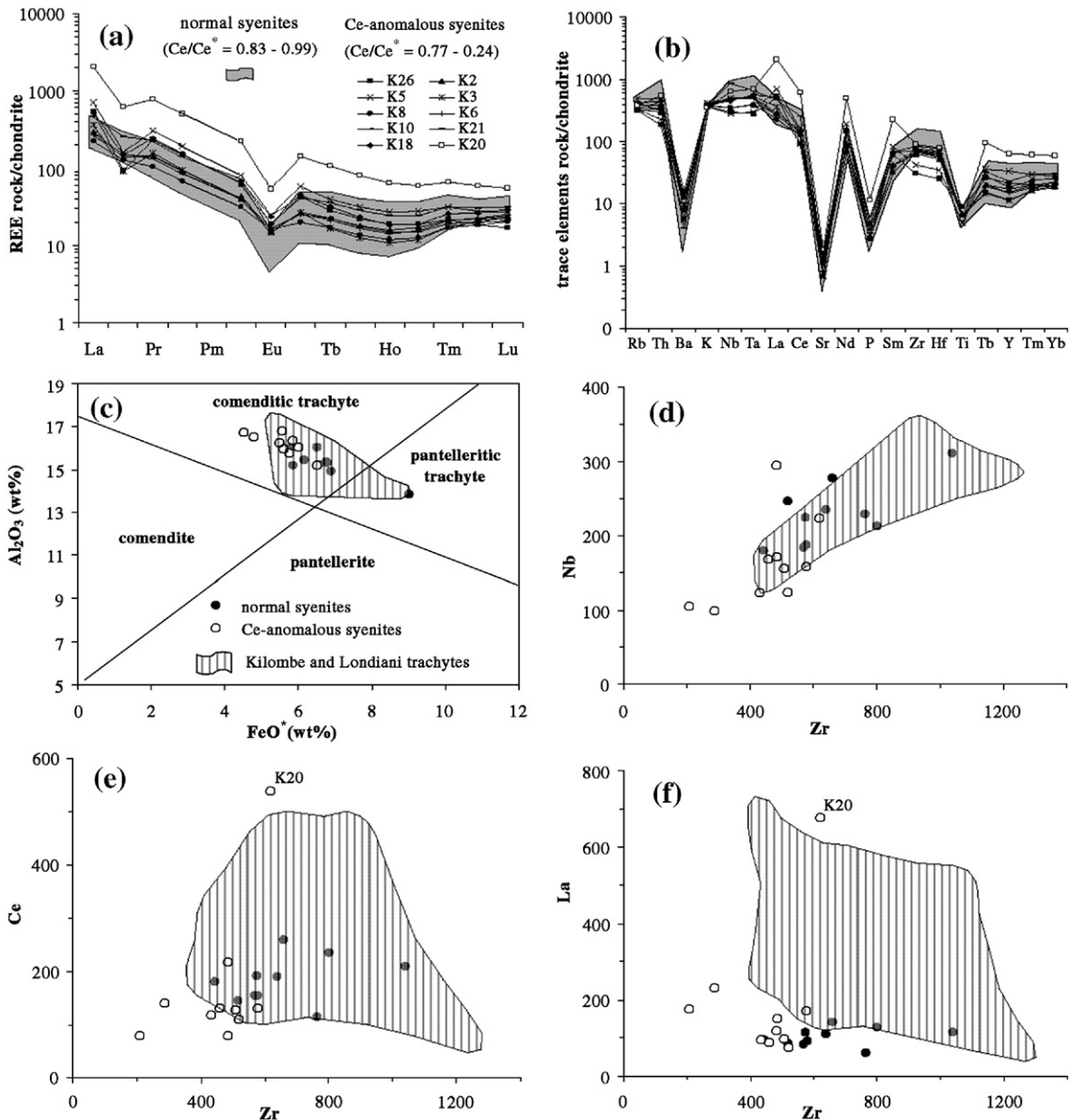
Fig. 7. (a) Whole-rock REE and (b) incompatible trace element patterns normalized to chondrites (Nakamura, 1974; Thompson, 1982, respectively); (c) FeO*–Al_2O_3 classification diagram for SiO_2-saturated peralkaline trachytes and rhyolites (Macdonald, 1974); binary diagrams reporting (d) Nb, (e) Ce and (f) La vs. Zr of the two syenite groups of Kilombe as concerning the Ce-anomaly (syenite symbols as in c). The fields covered by Kilombe and Londiani trachytes (Jones, 1981) are shown in (c–f).

6. Whole-rock geochemistry: magmatic vs. post-magmatic features

Major oxides and some whole-rock geochemical normative parameters of the autoliths are reported in Table 4. Electronic Supplement 1 also provides complete CIPW norms and trace element data. In order to emphasize the post-magmatic alteration processes, samples of Kilombe have been further divided into two groups: (i) "normal" syenites, with Ce/Ce* ratios between 0.83 and 0.99, and (ii) Ce-anomalous syenites with marked negative Ce-anomalies (Ce/Ce* 0.77–0.24; Table 4 and Fig. 7a). All the syenites are weakly peralkaline, with their peralkalinity index (PI; $(Na_2O+K_2O)/Al_2O_3$ molar ratio) ranging from 1.01 to 1.26. CIPW norms, calculated assuming an $Fe_2O_3/(Fe_2O_3+FeO)$ ratio of 0.5, as recommended by Middlemost (1989) for trachytic rocks, reflect the petrographic evidence that the syenites straddle the critical line of silica undersaturation (alkali feldspar join in the "residuum system"; ne 0–1% to qz 0–0.8%). Sample K24, with ∼2% modal analcime, has neither ne nor qz (Tables 1 and 4).

Major element compositions of the syenites from Kilombe and Londiani are similar to those of trachyte lavas from these centres (Jones, 1979a), although the latter have slightly higher TiO_2, MgO, CaO and P_2O_5. In contrast, the incompatible trace elements, such as Zr, Nb and Y, tend to have lower abundances in the syenites, prompting Jones (1979a) to suggest that the crystallization of the syenites did not go to completion but that a small volume of residual liquid escaped from the crystal mush.

The cogenetic relations between the Kilombe and Londiani trachytes, and the silica-saturated syenites of Kilombe are shown on an FeO* vs. Al_2O_3 plot (Fig. 7c). Magmas yielding the "normal" syenites (as regards Ce content) evolved from comenditic to pantelleritic trachyte compositions, whilst the Ce-anomalous syenites reflect only the composition of comenditic trachytes. Both types of syenite have significant negative Eu anomalies (Eu/Eu*=0.24–0.63; Table 4, Fig. 7a), suggesting significant fractional crystallization of plagioclase. Negative anomalies of Ba, Sr, Ti and P in a chondrite-normalized incompatible element plot (Fig. 7b) also indicate an ancestry involving plagioclase, Fe–Ti oxides and apatite fractionation. There is considerable overlap in trace element concentrations between the two syenite types, although LREE, Ba and Sr reach higher abundances in the Ce-anomalous syenites, whereas the "normal" syenites can have higher contents of Nb, Ta, Th, Zr and Hf (Fig. 7b, Supplement 1).

Nb vs. Zr, Ce vs. Zr and La vs. Zr diagrams for both syenite groups and Kilombe–Londiani trachytes are presented in Fig. 7d–f. In both types of syenites and trachytes, Zr, Nb and the most incompatible elements (such as Th, Hf, Rb and Ta) generally show positive correlations with each other (Fig. 7d; Supplement 1). In the syenites, this positive correlation is also shown by Ce (Fig. 7e) whereas the trachytes, as already emphasized by Jones (1979a), do not show any trend for all of the LREE (Figs. 7e, f). However, with the exception of Ce, LREE (here, for instance, La; Fig. 7f) in the syenites are characterised by slightly decreasing patterns. In the Ce-anomalous syenite autolith K20, the REE_2O_3 content is at least three times higher than in the other syenites (Table 4; Fig. 7a, e, f).

It is concluded that some processes have selectively affected the LREE concentrations in both syenite autoliths and trachytes.

7. Discussion

7.1. Stages of crystallization

The main stages of magmatic crystallization of both silica-undersaturated and silica-saturated samples can be categorized as (1) early crystallization, (2) main growth, and (3) late-interstitial crystallization (Fig. 8). Early growth of alkali feldspars was accompanied by the crystallization of fayalite, Fe–Ti oxides, apatite, Mg–hedenbergite and phyllosilicates (now very altered). Fayalite occurs exclusively in the silica-saturated syenites and, since it is typically an early crystallising phase and is not present within the alkali feldspars, we infer its crystallization pre-dated the onset of alkali feldspar nucleation.

The main growth stage involved crystallization of alkali feldspars, Fe–Ti oxides, apatite and pyroxenes (in the sequence Mg–hedenbergite → aegirine–augite ± Ca–aegirine). However, there was subordinate growth of amphibole (katophorite to arfvedsonite), annite, aenigmatite, monazite, zircon, chevkinite–(Ce), thorite, pyrochlore and xenotime, which became included in the growing feldspars. Mineral reaction/overgrowth processes that started during the main growth stage and persisted into the late-interstitial one were responsible for the replacement of (i) Mg–hedenbergite by sodium pyroxenes, (ii) fayalite by amphiboles, (iii) magnetite by aenigmatite and (iv) K by Na in the alkali feldspars (Fig. 8). Exsolution in the Ti–magnetites of the silica-saturated syenites is inferred to have been promoted by circulating fluids. In contrast, the absence of exsolution in the silica-undersaturated syenites may be attributed to their having been ejected shortly after completion of crystallization.
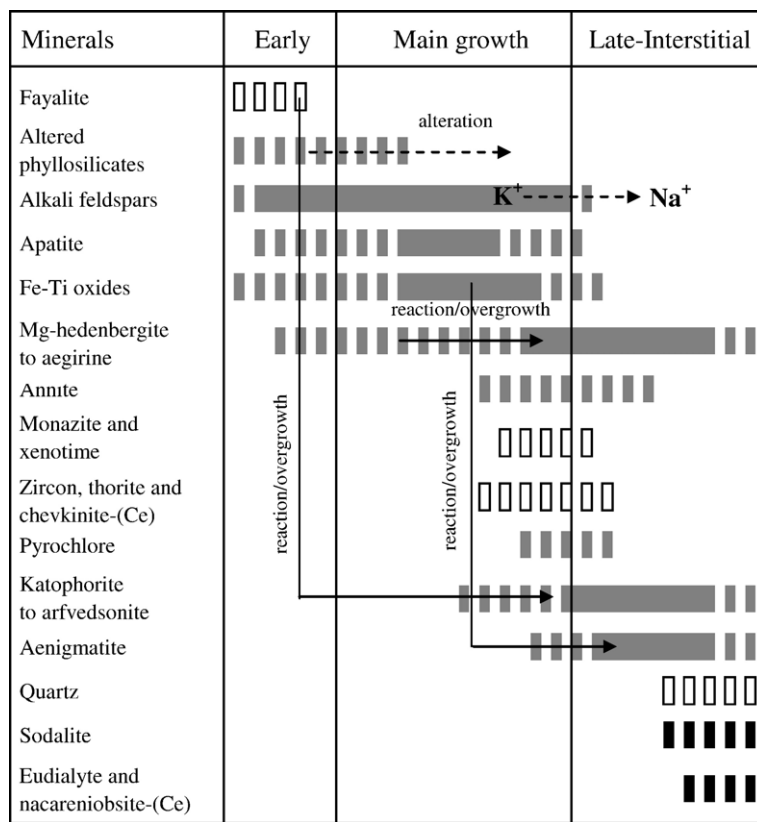
Fig. 8. Bar diagram showing the evolutionary stages of crystallization in the syenite autoliths (grey bands). Diversification of mineral occurrences in the silica-undersaturated (black) and silica-saturated syenites (white) is also shown.

The overwhelmingly dominant crystallization of plagioclase produced a peralkaline residual liquid enriched in volatiles, sodium and incompatible trace elements. Minerals whose growth continued into the late crystallization stage include pyroxenes (from aegirine–augite to aegirine), amphiboles, aenigmatite and annite. Pyrochlore in the silica-undersaturated syenites and minerals such as pyrochlore, monazite, xenotime, chevkinite–(Ce), zircon and thorite in the silica-saturated samples indicate that the magmas did not become saturated in HFSE and REE until the late growth of feldspar (Table 1; Fig. 8). Eudialyte, nacareniobsite–(Ce) and sodalite in the silica-under-saturated, and quartz in the silica-saturated syenites, are inferred to have been the latest magmatic phases to crystallize, since they do not occur as inclusions in other minerals (Fig. 8).

7.2. Phase equilibria and origin of hydrothermal fluids

Because of the relatively high degree of alteration of the silica-saturated syenites, geothermobarometric programs such as QUILF (e.g., Marks and Markl, 2001) cannot be used. For the sodalite-bearing syenites, ilmenite–magnetite equilibria (Andersen and Lindsley, 1985) indicate f_{O_2} between -19.5 and -23.1 log units at $T=679$–578 °C, slightly below the synthetic FMQ buffer (Fig. 9). The subsequent crystallization of aenigmatite and Na-rich pyroxenes may indicate an increase of oxidation state in the late-magmatic liquids and implies interaction with post-magmatic fluids (Marks et al., 2003). Different Ca, Na and F contents and Fe^{3+}/Fe^{2+} ratios in the same amphibole crystals (Fig. 4) are also ascribed to fast and discontinuous changes of the solid/liquid equilibrium and volatile fugacity during the main growth/interstitial stages. Fluid interactions from the late-main growth stage onwards were also responsible for the (near-) simultaneous crystallization of Fe–Ti oxides, arfvedsonite, aenigmatite and aegirine, whose stability relationships are displayed in a log f_{O_2} vs. T diagram (Fig. 9).

The study of fluid inclusions and REE patterns in the monazite and parisite–bastnaesite minerals of the Bayan
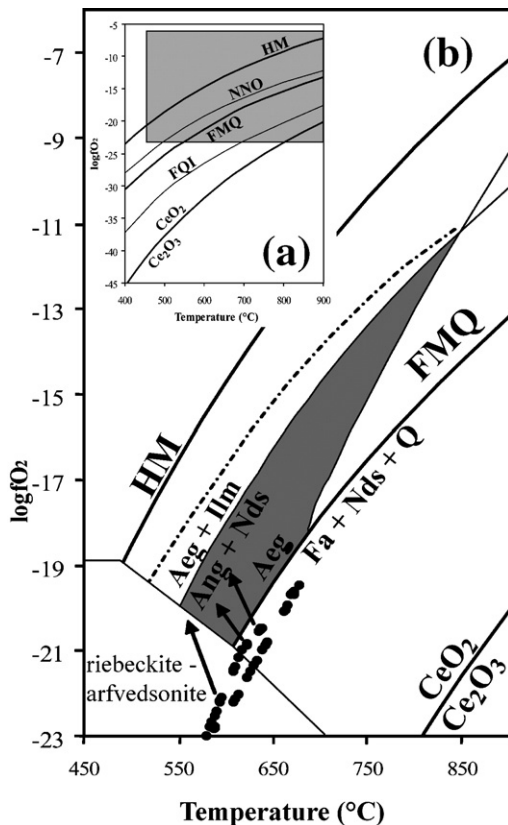
Fig. 9. (a) log f_{O_2} vs. T diagram showing the calculated $2Ce_2O_3 + O_2 = 4CeO_2$ equilibrium curve; hematite–magnetite (HM), nickel–nickel oxide (NNO), fayalite–magnetite–quartz (FMQ) and fayalite–quartz–iron (FQI) buffers; (b) enlargement of the light-grey inset in (a) shows the ilmenite–magnetite equilibrium calculation (full circles) for the sodalite-bearing syenites, the no-oxides zone, i.e., the field of aenigmatite stability (dark grey) and the upper limit of riebeckite–arfvedsonite amphiboles (after Nicholls and Carmichael, 1969). The arrows indicate the proposed intermittent f_{O_2} shifts during the cooling history of the trachytic magmas at the upper margins of the Kilombe magma chamber. Aeg=aegirine, Ilm=ilmenite, Ang=aenigmatite, Fa=fayalite, Q=quartz, Nds=Na-disilicate.

Obo deposit (Inner Mongolia) indicated that REE partitioning is correlated with the molar fraction of CO_2 and temperature of the hydrothermal fluids (Smith et al., 2000). The occurrence of REE complexes in low-temperature and H_2O-rich fluids typically increases with atomic number leading to higher MREE solubility. The mineralization of REE–fluorcarbonates and monazite with La/Nd$_N$ ratios <2 takes place in dominant aqueous solutions at low temperature (minimum estimates of 150–250 °C, <10 MPa), whereas La/Nd$_N$>4 is inferred at higher temperatures (230–280 °C, 8–10 MPa) and relatively high XCO$_2$ (up to 0.84) of the mineralizing fluids. Fig. 10 shows the Ce/Ce* vs. La/Nd$_N$ ratios in the monazite, synchysite–bastnaesite minerals and syenites

of Kilombe. In the syenites decrease in Ce/Ce* is accompanied by a general increase in La/Nd$_N$ from 2.7 to 4.1 (Table 4). Synchysite–bastnaesite minerals show two distinct groups that could reflect the composition of two types of mineralizing fluids. A low-temperature H_2O-rich fluid yielded high Ce/Ce* (0.74–0.85) and low La/Nd$_N$ REE–fluorcarbonate compositions (2.0–3.9), and a higher temperature CO_2-rich fluid promoted crystallization of synchysite–bastnaesite minerals with lower Ce/Ce* (0.43–0.52) and higher La/Nd$_N$ ratios (5.1–7.2). In Fig. 10, syenites with the lowest Ce/Ce* are very close to the REE–fluorcarbonates group inferred to have crystallized from CO_2-rich hydrothermal fluids. Monazites show more scattered patterns because they were probably affected by magmatic REE fractionation. This would indicate that the relatively low Ce values displayed by whole-rock compositions, monazites and REE–fluorcarbonate minerals were largely controlled by the amounts of CO_2 in the post-magmatic fluids.

Lumpkin and Ewing (1995) recognized three types of alteration of the pyrochlore subgroup in nepheline syenites and carbonatites: (1) primary alteration represented by the substitutions $^{A}Na^{Y}F \rightarrow {^{A}}\square \ ^{Y}\square$ and $^{A}Ca^{Y}O \rightarrow {^{A}}\square \ ^{Y}\square$ ($\square$=vacancies) promoted by a fluid-phase at ~300–550 °C; (2) secondary alteration (<150 °C) characterized by the same replacement
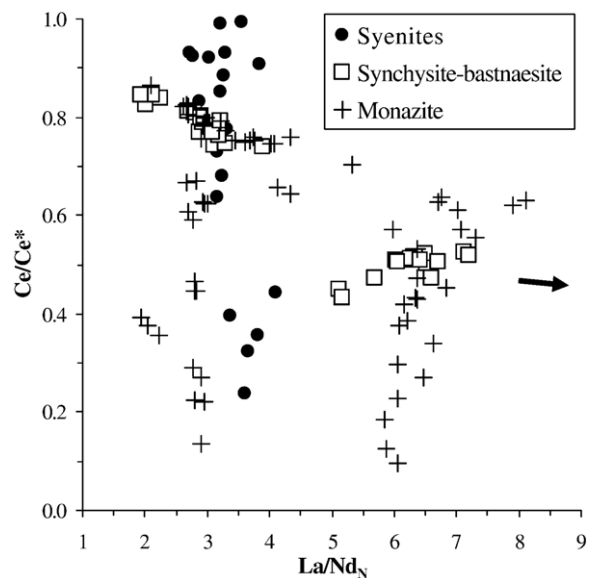
Fig. 10. Ce/Ce* vs. La/Nd$_N$ diagram for the syenites, REE–fluorcarbonates (synchysite–bastnaesite) and monazites. The black arrow indicate two monazite spot analyses with La/Nd$_N$ of 14.3 and 18.0.

reactions, plus $^ACa^XO \rightarrow ^A\square \ ^X\square$, and extreme hydration (10–15 wt.% H_2O or 2–3 molecules pfu); (3) transitional alteration between the two (200–350 °C). Alteration patterns of the Kilombe pyrochlores vary between primary and transitional (Fig. 11). In Fig. 11 the secondary alteration pattern (<150 °C) has been omitted. The sodalite-bearing sample K16 is the only one showing only primary alteration trends in accordance with the inference that the sodalite-bearing autoliths were ejected shortly after complete solidification. By contrast, all the silica-saturated samples show lower temperature patterns that can be related to fluids retaining a secondary component.

One silica-saturated sample, K24, with neither qz nor ne in the norm (Table 4), has bastnaesite enclosed

in analcime that fills the space between alkali feldspars (Fig. 5f). We infer that this syenite crystallized from a qz-normative magma and lost SiO_2 due to the post-magmatic crystallization of analcime. The simultaneous crystallization of bastnaesite and analcime strongly supports a hydrothermal origin of the feldspathoid.

Since pyrochlores of Kilombe underwent both primary and transitional alteration (sensu Lumpkin and Ewing, 1995), the temperature of the hydrothermal fluids can be roughly constrained within the range 200–550 °C. LREE variations in the synchysite–bastnaesite minerals indicate that a higher temperature (>250 °C) can be inferred for fluids with relatively high XCO_2.

The model proposed here contends that fluids enriched in CO_2, F, Na, Ca, REE (mainly lanthanides), and subordinately in H_2O, Mn, Pb and P, interacted with the silica-saturated syenites that had crystallized in the magma chamber. Such fluids were depleted in Ce and are very similar to differentiated carbonatitic fluids with negative Ce-anomalies. Positive Ce-anomalies are commonly observed in the magmatic cerian pyrochlores of carbonatites (e.g., Hogarth et al., 1988; Hornig-Kjarsgaard, 1998; Wagner et al., 2003), whilst negative ones are found only in pyrochlore-free carbonatites (Hornig-Kjarsgaard, 1998). Hornig-Kjarsgaard (1998) indicated that the fractionation of positive Ce-anomalous pyrochlores from carbonatitic magmas can generate negative Ce-anomalous carbonatite liquids (and fluids).

Cerium is unique among the rare-earth elements in being able to display tetravalence. The positive anomaly in the cerian pyrochlores has been attributed to substitution of Ce^{4+} for REE^{3+} in the pyrochlore structure (Eby, 1975). We agree with this inference and believe that the incorporation of Ce^{4+} occurs in place of Nb^{5+} and Ti^{4+} in the B site of pyrochlore. Indeed, the ionic potential (i.e., z/r) and ionic ratio (r) of tetravalent Ce (z/r=3.96 Å^{-1}, r=1.01 Å) are closer to Nb^{5+} (z/r=7.14 Å^{-1}, r=0.70 Å) and Ti^{4+} (z/r=5.88 Å^{-1}, r=0.68 Å) than Ca^{2+} (z/r=2.02 Å^{-1}, r=0.99 Å) and the main A site cations of pyrochlore (i.e., Na^+ and REE^{3+}). This supposes that trivalent lanthanides, such as La (z/r=2.61 Å^{-1}, r=1.15 Å) and Ce (z/r=2.70 Å^{-1}, r=1.11 Å) enter the A site in place of Ca, while Ce^{4+} can be better incorporated in the pyrochlore B site dominated by Nb and Ti.

The calculated CeO_2–Ce_2O_3 buffer curve indicates low oxygen fugacity (Fig. 9) well below the initial f_{O_2} of carbonatite magma, inferred to be as low as NNO (Bell, 1989, and reference therein). This is consistent with high Ce^{4+}/Ce^{3+} ratios in carbonatite magmas. An external source such as carbonatite fluids depleted in
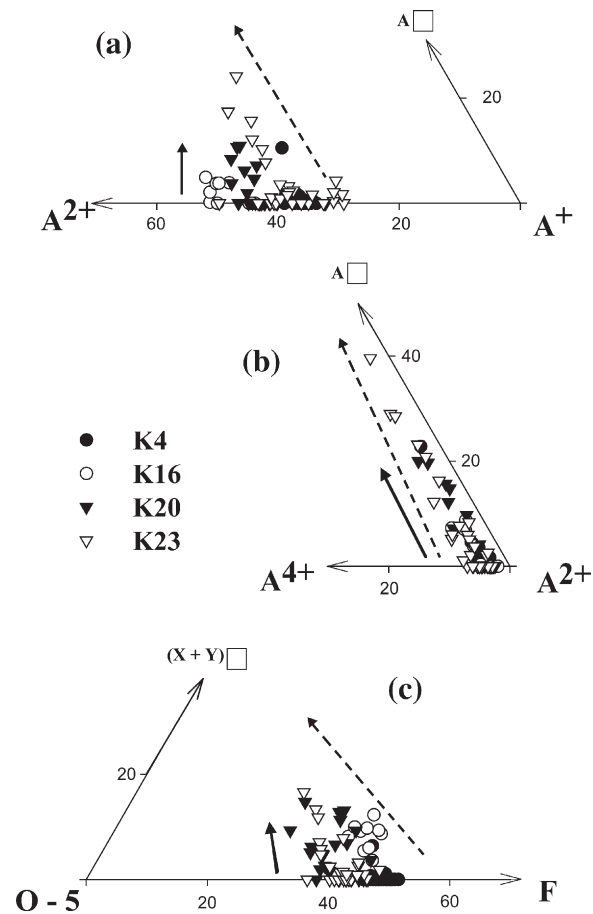

Fig. 11. Triangular plots for pyrochlores of Kilombe syenites: (a) divalent A-site cations, monovalent A-site cations and A-site vacancies; (b) tetravalent A-site cations, divalent A-site cations and A-site vacancies; (c) Oxygen (O)-5, F and X+Y anion vacancies. Primary (bold arrows) and transitional (broken arrows) alteration patterns from Lumpkin and Ewing (1995) are also shown.

Ce, because of the incorporation of tetravalent Ce into previously fractionated magmatic pyrochlores, could be the reason for the origin of the Ce-anomalous syenite autoliths.

8. Final remarks

The absence of post-magmatic alteration and magnetite exsolution in the sodalite-bearing samples indicates that they are the youngest syenites, ejected shortly after complete solidification. The presence of eudialyte and nacareniobsite–(Ce) along with ilmenite and magnetite allows them to be classified as transitional agpaitic syenites (sensu Sørensen, 1997).

The silica-saturated syenites are inferred to be older than the undersaturated varieties, having undergone longer interaction with syn-/post-magmatic fluids. Two main types of metasomatic fluids have been recognized: (i) aqueous fluids leading to the formation of clay minerals±analcime, and synchysite–bastnaesite minerals with low La/Nd$_N$, and (ii) CO_2-rich fluids that produced REE–fluorcarbonates with higher La/Nd$_N$ ratios, which were responsible for the alteration of primary and formation of secondary monazite group minerals. There is mounting evidence that trachytic magmatism in the Kenya Rift Valley was associated with carbonatitic magma (e.g., Scott, 1982; Macdonald et al., 1993; Hawkesworth et al., 2000). We argue that fractionation of positive Ce-anomalous pyrochlores from carbonatitic magmas generated Ce-depleted derivatives at Kilombe. It is inferred that a carbonatitic source at depth below(?) the trachytic chamber, released at intervals fluids that percolated into the overlying subvolcanic system. An alternative hypothesis is that carbonatite plutonic bodies constituting the trachytic magma chamber walls, or located near the replenishing conduit of such a subvolcanic system, were melted by the silicate magma and were able to move upwards through the chamber. Because of their low density and viscosity and high immiscibility with the silicate melts (e.g., Kjarsgaard et al., 1995; Petibon et al., 1998; Harmer, 1999; Srivastava et al., 2005), these postulated carbonatitic fluids/liquids were able to reach the chamber roof and walls where they interacted with the crystallizing peralkaline trachytic melts in the compositional boundary layer.

Accessory phases of the studied syenites, including eudialyte, nacareniobsite–(Ce), chevkinite–(Ce), pyrochlore, monazite, synchysite–bastnaesite solid solutions and thorite, are all recorded here for the first time from Kilombe and possibly from many of the Quaternary trachytic volcanoes of the Kenya rift. We believe also that this is the first report of eudialyte, nacareniobsite–(Ce) and thorite in Kenya.

Appendix A. Supplementary data

Supplementary data associated with this article can be found, in the online version, at doi:10.1016/j.lithos.2006.03.026.

References

Abbott, M.J., 1967. Aenigmatite from the groundmass of a peralkaline trachyte. Am. Mineral. 52, 1895–1901.

Andersen, D.J., Lindsley, D.H., 1985. New (and final!) models for the Ti–magnetite/ilmenite geothermometer and oxygen barometer. Eos Trans. Am. Geophys. Union 66 (18). 416 pp.

Bell, K. (Ed.), 1989. Carbonatites: Genesis and Evolution. Unwin Hypman, London. 618 pp.

Bowie, S.H.U., Horne, J.E.T., 1953. Cheralite, a new mineral of the monazite group. Min. Mag. 30, 93–99.

Chakhmouradian, A.R., Mitchell, R.H., 1998. Lueshite, pyrochlore and monazite–(Ce) from apatite–dolomite carbonatite, Lesnaya Varaka complex, Kola Peninsula, Russia. Min. Mag. 62, 769–782.

Chakhmouradian, A.R., Mitchell, R.H., 2002. New data on pyrochlore- and perovskite-group minerals from the Lovozero alkaline complex, Russia. Eur. J. Mineral. 14, 821–836.

Chakhmouradian, A.R., Sitnikova, M.A., 1999. Radioactive minerals from murmanite–lorenzenite tinguaite at Mt. Selsurt, Lovozero complex, Kola Peninsula. Eur. J. Mineral. 11, 871–878.

Clarke, M.C.G., Woodhall, D.G., Allen, D., Darling, G., 1990. Geological, volcanological and hydrogeological controls on the occurrence of geothermal activity in the area surrounding Lake Naivasha, Kenya. Report. Nairobi: Ministry of Energy.

Dawson, J.B., 1997. Neogene–Recent rifting and volcanism in northern Tanzania: relevance for comparisons between the Gardar province and the East African Rift valley. Min. Mag. 61, 543–548.

Deer, W.A., Howie, R.A., Zussman, J. (Eds.), 1966. An Introduction to the Rock-Forming Minerals. Longman Group (FE) Limited (Prd.), London. 696 pp.

Della Ventura, G., Mottana, A., Parodi, G.C., Paudsepp, M., Bellatreccia, F., Caprilli, E., Rossi, P., Fiori, S., 1996. Monazite–huttonite solid-solutions from the Vico Volcanic Complex, Latium, Italy. Min. Mag. 60, 751–758.

Eby, G.N., 1975. Abundance and distribution of the rare earth elements and yttrium in the rocks and minerals of the Oka carbonatite complex, Quebec. Geochim. Cosmochim. Acta 39, 597–620.

Förster, H.J., 2000. Cerite–(Ce) and thorian synchysite–(Ce) from the Niederbobritzsch granite, Erzgebirge, Germany: implications for the differential mobility of the LREE and Th during alteration. Can. Mineral. 38, 67–79.

Harmer, R.E., 1999. The petrogenetic association of carbonatite and alkaline magmatism: constraints from the Spitskop Complex, South Africa. J. Petrol. 40, 525–548.

Hawkesworth, C.J., Blake, S., Evans, P., Hughes, R., Macdonald, R., Thomas, L.E., Turner, S.P., Zellmer, G., 2000. Time scales of crystal fractionation in magma chambers—integrating physical, isotopic and geochemical perspectives. J. Petrol. 41, 991–1006.

Hogarth, D.D., 1977. Classification and nomenclature of the pyrochlore group. Am. Mineral. 63, 757–761.

Hogarth, D.D., 1989. Pyrochlore, apatite and amphibole: distinctive minerals in carbonatite. In: Bell, K. (Ed.), Carbonatites: Genesis and Evolution. Unwin Hyman, London, pp. 105–148.

Hogarth, D.D., Rushforth, P., McKorkell, R.H., 1988. The Blackburn carbonatites, near Ottawa, Ontario: dikes with fluidized emplacement. Can. Mineral. 26, 377–390.

Hornig-Kjarsgaard, I., 1998. Rare earth elements in sövitic carbonatites and their mineral phases. J. Petrol. 39 (11–12), 2105–2121.

Isobe, H., 2000. Hydrothermal synthesis experimental and phase relations of rare earth fluorocarbonate minerals. Abstr. Programs-Geol. Soc. Am. 32 (7). 144 pp.

Johnsen, O., Gault, R.A., 1997. Chemical variation in eudialyte. Neues Jahrb. Mineral. 171 (3), 215–237.

Johnsen, O., Grice, J.D., 1999. The crystal chemistry of the eudialyte group. Can. Mineral. 37, 865–891.

Johnsen, O., Grice, J.D., Gault, R.A., 1998. Kentbrooksite from the Kangerdlugssuaq intrusion, East Greenland, a new Mn–REE–Nb–F end-member in a series within the eudialyte group: description and crystal structure. Eur. J. Mineral. 10, 207–219.

Johnsen, O., Grice, J.D., Gault, R.A., 2001. The eudialyte group: a review. Geol. Greenl. Surv. Bull. 190, 65–72.

Jones, W.B., 1979a. Syenite boulders associated with Kenyan trachyte volcanoes. Lithos 12, 89–97.

Jones, W.B., 1979b. Mixed benmoreite/trachyte flows from Kenya and their bearing on the Daly gap. Geol. Mag. 116, 487–489.

Jones, W.B., 1981. Chemical effects of deuteric alteration in some Kenyan trachyte lavas. Mineral. Mag. 44, 279–285.

Khomyakov, A.P., 1995. Mineralogy of Hyperagpaitic Alkaline Rocks. Oxford Science Publications. 222 pp.

Kjarsgaard, B.A., Hamilton, D.L., Peterson, T.D., 1995. Peralkaline nephelinite/carbonatite liquid immiscibility: comparison of phase compositions in experiments and natural lavas from Oldoinyo Lengai. In: Bell, K., Keller, J. (Eds.), Carbonatite Volcanism: Oldoinyo Lengai and the Petrogenesis of Natrocarbonatites. LAVCEI Proceed. Volcanol., vol. 4. Springer-Verlag, Berlin, pp. 163–190.

Kovalenko, V.I., Tsaryeva, A.V., Goreglyad, A.V., Yarmolyuk, V.V., Troitsky, V.A., Hervig, R.L., Farmer, G.L., 1995. The peralkaline granite-related Khaldzan–Buregtey rare metal (Zr, Nb, REE) deposit, Western Mongolia. Econ. Geol. 90, 530–547.

Kunzmann, T., 1999. The aenigmatite–rhönite mineral group. Eur. J. Mineral. 11, 743–756.

Leake, B.E., Woolley, A.R., Arps, C.E.S., Birch, W.D., Gilbert, M.C., Grice, J.D., Hawthorne, F.C., Kato, A., Kisch, H.J., Krivovichev, V.G., Linthout, K., Laird, J., Mandarino, J., Maresch, W.V., Nickel, E.H., Schumaker, J.C., Smith, D.C., Stephenson, N.C.N., Ungaretti, L., Whittaker, E.J.W., Youzhi, G., 1997. Nomenclature of amphiboles: report of the Subcommittee on Amphiboles of the International Mineralogical Association Commission on New Minerals and Mineral Names. Min. Mag. 61, 295–321.

Leat, P.T., Macdonald, R., Smith, R.L., 1984. Geochemical evolution of the Menengai caldera volcano. J. Geophys. Res. 89, 8571–8592.

Lumpkin, G.R., Ewing, R.C., 1995. Geochemical alteration of pyrochlore group minerals: pyrochlore subgroup. Am. Mineral. 80, 732–743.

Lumpkin, G.R., Ewing, R.C., 1996. Geochemical alteration of pyrochlore group minerals: betafite subgroup. Am. Mineral. 81, 1237–1248.

Macdonald, R., 1974. Nomenclature and petrochemistry of the peralkaline oversaturated extrusive rocks. Bull. Volcanol. 38, 498–516.

Macdonald, R., 1987. Quaternary peralkaline silicic rocks and caldera volcanoes of Kenya. In: Fitton, J.G., Upton, B.G.J. (Eds.), Alkaline Igneous Rocks. Spec. Publ.-Geol. Soc. Lond., vol. 30, pp. 313–333.

Macdonald, R., 1994. Petrological evidence regarding the evolution of the Kenya Rift valley. Tectonophysics 236, 373–390.

Macdonald, R., Belkin, H.E., 2002. Compositional variation in minerals of the chevkinite group. Mineral. Mag. 66, 1075–1098.

Macdonald, R., Davies, G.R., Bliss, C.M., Leat, P.T., Bailey, D.K., Smith, R.L., 1987. Geochemistry of high-silica peralkaline rhyolites, Naivasha Kenya rift valley. J. Petrol. 28, 979–1008.

Macdonald, R., Kjarsgaard, B.A., Skilling, I.P., Davies, G.R., Hamilton, D.L., Black, S., 1993. Liquid immiscibility between trachyte and carbonate in ash flow tuffs from Kenya. Contrib. Mineral. Petrol. 114, 276–287.

Macdonald, R., Navarro, J.-M., Upton, B.G.J., Davies, G.R., 1994. Strong compositional zonation in peralkaline magma: Menengai, Kenya Rift valley. J. Volcanol. Geotherm. Res. 60, 301–325.

Marks, M., Markl, G., 2001. Fractionation and assimilation processes in the alkaline augite syenite unit of the Ilímaussaq Intrusion, South Greenland, as deduced from phase equilibria. J. Petrol. 42, 1947–1969.

Marks, M., Vennemann, T., Siebel, W., Markl, G., 2003. Quantification of magmatic and hydrothermal processes in a peralkaline syenite–alkali granite complex based on textures, phase equilibria, and stable and radiogenic isotopes. J. Petrol. 44, 1247–1280.

McCall, G.J.H., 1964. Kilombe caldera, Kenya. Proc. Geol. Assoc. 75, 565–572.

Middlemost, E.A.K., 1989. Iron oxidation ratios, norms and classification of volcanic rocks. Chem. Geol. 77, 19–26.

Nakamura, N., 1974. Determination of REE, Ba, Fe, Mg, Na and K in carbonaceous and ordinary chondrites. Geochim. Cosmochim. Acta 38, 757–775.

Nicholls, J., Carmichael, I.S.E., 1969. Peralkaline acid liquids: a petrological study. Contrib. Mineral. Petrol. 20, 268–294.

Onuonga, I.O., Bowden, P., 2000. Hot-spring and supergene lanthanide mineralization at the Buru carbonatite centre, Western Kenya. Mineral. Mag. 64, 663–673.

Petersen, O.V., Rønsbo, J.G., Leonardsen, E.S., 1989. Nacareniobsite–(Ce), a new mineral species from the Ilímaussaq alkaline complex, South Greenland, and its relation to mosandrite and the rinkite series. Neues Jahrb. Mineral. 2, 84–96.

Petibon, C.M., Kjarsgaard, B.A., Jenner, G.A., Jackson, S.E., 1998. Phase relationships of a silicate-bearing natrocarbonatite from Oldoinyo Lengai at 20 and 100 MPa. J. Petrol. 39 (11–12), 2137–2151.

Pointer, C.M., Ashworth, J.R., Ixer, R.A., 1988. The zircon–thorite mineral group in metasomatized granite, Ririwai, Nigeria 1. Geochemistry and metastable solid solution of thorite. Mineral. Petrol. 38, 245–262.

Rieder, M., Cavazzini, G., D'Yakonov, Y.S., Frank-Kamenetskii, V.A., Gottardi, G., Guggenheim, S., Koval, P.V., Müller, G., Neiva, A.M.R., Radoslovich, E.W., Robert, J.L., Sassi, F.P., Takeda, H., Weiss, Z., Wones, D.R., 1998. Nomenclature of the micas. Can. Mineral. 36, 905–912.

Ridolfi, F., 2004. Minerali contenenti terre rare (REE) ed elementi ad alta forza di campo (HFSE) nelle sieniti peralcaline: cristallochimica e significato petrogenetico. Unpublished Doctoral thesis. 234 pp.

Ridolfi, F., Renzulli, A., Santi, P., Upton, B.G.J., 2003. Evolutionary stages of crystallization of weakly peralkaline syenites: evidence from ejecta in the plinian deposits of Agua de Pau volcano (São Miguel, Azores Islands). Min. Mag. 67, 749–767.

Rock, N.M.S., 1990. The International Mineralogical Association (IMA/CNMMN) pyroxene nomenclature scheme: computerization and its consequences. Mineral. Petrol. 43, 99–119.

Rogers, N.W., Evans, P.J., Blake, S., Scott, S.C., Hawkesworth, C.J., 2004. Rates and timescales of fractional crystallization from $^{238}U–^{230}Th–^{226}Ra$ disequilibria in trachyte lavas from Longonot volcano, Kenya. J. Petrol. 45, 1747–1776.

Scaillet, B., MacDonald, R., 2003. Experimental constraints on the relationships between peralkaline rhyolites of the Kenya Rift Valley. J. Petrol. 44, 1867–1894.

Scott, S.C., 1980. The geology of Longonot volcano, central Kenya: a question of volumes. Philos. Trans. R. Soc. Lond., A 296, 437–465.

Scott, S.C., 1982. Evidence from Longonot volcano, Central Kenya, lending further support to the argument for a coexisting CO_2 rich vapour in peralkaline magma. Geol. Mag. 119, 215–217.

Shelley, D., 1992. Igneous and Metamorphic Rocks under the Microscope. Chapman & Hall Ed. 161 pp.

Slepnev, Y.S., 1957. On minerals of the rinkite group. Izv. Akad. Nauk SSSR, Ser. Geol. 3, 63–75.

Smith, J.V., Brown, W.L., 1988. Feldspar Minerals, 2nd edn. (Vol. I). Springer-Verlag, Berlin. 824 pp.

Smith, M.P., Henderson, P., Campbell, L.S., 2000. Fractionation of the REE during hydrothermal processes: constraints from the Bayan Obo Fe–REE–Nb deposit, Inner Mongolia, China. Geochim. Cosmochim. Acta 64, 3141–3160.

Sørensen, H., 1997. The agpaitic rocks–an overview. Mineral. Mag. 61, 485–498.

Srivastava, R.K., Heaman, L.M., Sinha, A.K., Shihua, S., 2005. Emplacement age and isotope geochemistry of Sung Valley alkaline–carbonatite complex, Shillong Plateau, northeastern India: implications for primary carbonate melt and genesis of the associated silicate rocks. Lithos 81, 33–54.

Stähle, V., Koch, M., McCammon, C.A., 2002. Occurrence of low-Ti and high Ti freudenbergite in alkali syenite dikes from the Katzenbuckel volcano, Southwestern Germany. Can. Mineral. 40, 1609–1627.

Stromeyer, F., 1819. Summary of meeting 16 December 1819 [Fossilien…]. Gött. Gel. Anz. 3, 1993–2003.

Thompson, R.N., 1982. Magmatism of the British Tertiary Province. Scott. J. Geol. 18, 49–107.

Uher, P., Èerný, P., Chapman, R., Határ, J., Miko, O., 1998. Evolution of Nb, Ta-oxide minerals in the Prasiva granitic pegmatites, Slovakia: II. External hydrothermal Pb, Sb overprint. Can. Mineral. 36, 535–545.

Wagner, C., Mokhtari, A., Deloule, E., Chabaux, F., 2003. Carbonatite and alkaline magmatism in Taourirt (Morocco): petrological, geochemical and Sr–Nd isotope characteristics. J. Petrol. 44 (5), 937–965.

Wallace, G.M., Whalen, J.B., Martin, R.F., 1990. Agpaitic and miaskitic nepheline syenites of the McGerrigle plutonic complex, Gaspé, Quebec: an unusual petrological association. Can. Mineral. 28, 251–266.

Wolff, J.A., 1987. Crystallisation of nepheline syenite in a subvolcanic magma system: Tenerife, Canary Islands. Lithos 20, 207–223.